

## Invited Article: Attosecond photonics: Synthesis and control of light transients

M. Th. Hassan,<sup>1</sup> A. Wirth,<sup>1</sup> I. Grguraš,<sup>1</sup> A. Moulet,<sup>1</sup> T. T. Luu,<sup>1</sup> J. Gagnon,<sup>1</sup> V. Pervak,<sup>1,2</sup> and E. Goulielmakis<sup>1,a)</sup>

<sup>1</sup>Max-Planck-Institut für Quantenoptik, Hans-Kopfermann-Strasse 1, D-85748 Garching, Germany

<sup>2</sup>Department für Physik, Ludwig-Maximilians-Universität, Am Coulombwall 1, D-85748 Garching, Germany

(Received 28 March 2012; accepted 22 July 2012; published online 2 November 2012)

Ultimate control over light entails the capability of crafting its field waveform. Here, we detail the technological advances that have recently permitted the synthesis of light transients confinable to less than a single oscillation of its carrier wave and the precise attosecond tailoring of their fields. Our work opens the door to light field based control of electrons on the atomic, molecular, and mesoscopic scales. © 2012 American Institute of Physics. [<http://dx.doi.org/10.1063/1.4758310>]

### I. INTRODUCTION

Light, as a tool, has revolutionized the way we explore and control the microcosm. By manipulating its time-averaged properties, modern microscopes or spectroscopic devices operating in the visible, the near infrared, the ultraviolet, or the x-ray range of the electromagnetic spectrum can now attain a resolution fine enough to explore the structure of matter with exquisite detail: down to the level of single molecules and atoms. Light is also a key tool for the study and manipulation of dynamical phenomena of the microcosm if its control is extended to the temporal domain. Groundbreaking achievements in chronoscopy, spanning from the pioneering experiments of Abraham and Lemoine—in which electric spark-induced incoherent flashes of light were used to explore the Kerr response of matter<sup>1</sup>—to the most innovative studies and applications enabled by the use of ultrashort coherent laser pulses,<sup>2</sup> such as phenomena pertaining to molecular rotation, or the motion of atoms inside molecules or solids,<sup>3,4</sup> or even phenomena induced by electronic motions in atoms and molecules,<sup>5–9</sup> have unambiguously led to the conclusion that the finer the degree of control over the temporal properties of light, the higher is the attainable resolution for tracing or driving dynamical processes in the microcosm. Indeed, over the last 50 years the temporal resolution afforded by laser technology has advanced through 12 orders of magnitude from the microsecond to the attosecond time scale.

Restricting the emission of incoherent light bursts—via an electrically induced spark—to a roughly predefined time interval (Fig. 1(a)) is, in a sense, the precursor of modern temporal control of light, with the accuracy of this confinement roughly equal to the time it takes an electric discharge through a dilute gas in order to create a light flash. The invention of coherent light sources, the lasers,<sup>2</sup> sparked the development of more generic and sophisticated types of temporal control of light. One of the most popular techniques is pulse shaping and deals with the “on-demand” tailoring of cycle-averaged properties of a light pulse (Fig. 1(b)), such as the

temporal intensity profile (envelope) or the carrier frequency sweep across it (chirp). Pulse shaping has been extensively exercised on picosecond<sup>10</sup> and femtosecond scales.<sup>11</sup> In its most basic guise, it can be realized by tuning the temporal profile of a pulse using a prism-based<sup>12</sup> or grating-based<sup>13</sup> compression module, which is designed to adjust the chirp within a range of predefined settings that depend upon geometrical or dispersive properties—i.e. the distance between two prisms or the type of material composing them. Moreover, a more elaborate adjustment of the above properties is possible through the use of femtosecond pulse shapers. These devices exploit spatial light modulators<sup>14–16</sup> or acousto-optic programmable dispersive filters<sup>17</sup> in order to tune the spectral phase or the amplitude of a pulse (Fig. 1(b)), allowing to craft nearly arbitrary patterns on its temporal profile or even its polarization state.<sup>18</sup> Shaped pulses have been of fundamental importance for the practical implementation of quantum control<sup>19,20</sup> of matter: the exploitation of interference phenomena in the time and the frequency domain in order to guide the evolution of vibrational and rotational wavepackets in complex molecular systems and to steer chemical reactions to predefined paths or products.<sup>21–23</sup>

The control of cycle-integrated quantities of laser pulses attainable by the techniques of pulse shaping is still a subset of what can possibly be regarded as the ultimate control of classical light which is the direct tailoring of its instantaneous field vector through the precise sculpting and measurement (briefly: the synthesis) of its subcycle temporal profile. Steps in this direction have required the advancement of pulsed light's coherence properties to a new level to ensure that laser light pulses are produced with identical field characteristics. Specifically, even though trains of pulses emerging from modern lasers have nearly identical spectral density and phase, they suffer a pulse-to-pulse phase drift of their field carrier with respect to their intensity envelope  $\phi_{CE}$ . Sources of this “carrier-envelope incoherence” are both the phase drift resulting from the difference in the group and the phase velocity of pulses in a laser oscillator due to material dispersion, as well as external noise.<sup>24</sup> Essential steps towards light field control include the measurement<sup>25</sup> of  $\phi_{CE}$  as well as its precise adjustment.<sup>26–31</sup> State-of-the-art waveform stabilization

<sup>a)</sup> Author to whom correspondence should be addressed. Electronic mail: elgo@mpq.mpg.de.

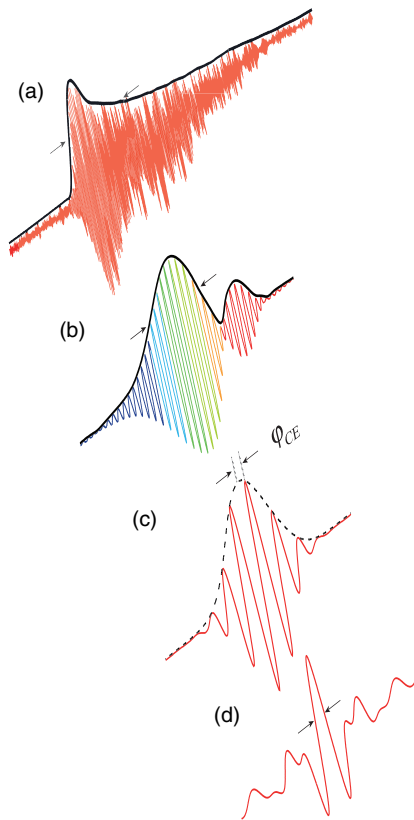


FIG. 1. Evolution of temporal control of light. Arrows denote the dynamical properties under control. (a) Confinement of light to incoherent flashes. (b) Femtosecond pulse shaping: control of cycle-integrated quantities of a light waveform. (c) Carrier envelope phase control of few-cycle pulses. (d) Subfemtosecond tailoring of light transients.

techniques have recently reduced the carrier envelope phase noise between consecutive pulses in a train to be lower than  $\sim 30$  mrad.<sup>30</sup>

The adjustment of  $\phi_{CE}$  can profoundly influence the sub-cycle evolution of the pulse (Fig. 1(c))—manifested by the controlled variation of the relative instantaneous intensity of adjacent field crests—as long as the envelope of the pulse varies quickly in relation to the field oscillations. This condition is easily fulfilled with pulses of a duration  $\sim 5$  fs or shorter carried at the near infrared range ( $\lambda_0 \sim 800$  nm,  $T_0 \sim 2.66$  fs). The difference between group and phase velocity of a pulse transmitted through a medium can be used to control or introduce the required offset  $\phi_{CE}$ . A carrier envelope phase shift of  $\sim \pi/2$ , for instance, requires the adjustment of the optical path of the pulse in fused silica by  $\sim 14.5$   $\mu\text{m}$  assuming a carrier wavelength of  $\lambda_0 = 800$  nm. This is typically possible using a pair of translatable wedges or a thin rotating optical slab inserted into the beam.

The amplification of  $\phi_{CE}$ -controlled few-cycle pulses to the terawatt power scale<sup>32</sup> opened the way to driving electronic processes with the field of light and has greatly influenced the advancement of attosecond science throughout its first decade. A detailed account of these achievements can be found in Ref. 33. Some of the most influential of these advances include the generation and measurement of EUV attosecond pulses,<sup>8,32,34</sup> the direct characterization of light

fields,<sup>35</sup> the direct tracing of inner<sup>7</sup> and valence shell electronic wavepackets,<sup>9</sup> ionization dynamics of atoms,<sup>36</sup> electron dynamics in molecular processes,<sup>37,38</sup> and the electron transport in solids.<sup>39</sup>

The precise adjustment of the carrier-envelope phase offset in few-cycle pulses offers an effective but still limited control knob for tuning the subcycle properties of light. Moreover, implementation of  $\phi_{CE}$  control relies on independent pulse compression strategies which so far work effectively for pulses with spectra spanning less than an optical octave. This imposes considerable limitations on the capability of controlling the field evolution of a pulse with subcycle or even attosecond precision as the latter requires control over super-octave light sources with pulse-to-pulse reproducible waveforms. This work aims at giving a detailed account of the technologies and techniques that have recently enabled the synthesis and subfemtosecond control of non-periodic super-octave light transients<sup>40</sup> spanning over more than 1.5 octaves in the visible (VIS), the near infrared (NIR), and ultraviolet (UV) ranges.

Previously, important results towards superoctave field synthesis could be attained only via the technique of molecular modulations.<sup>41–46</sup> This approach has recently permitted the subcycle shaping of optical fields via the superposition of quasi-monochromatic waves in the infrared and visible ranges.<sup>47</sup> Although these periodic waveforms are particularly important for advancing electronics to PHz frequencies, time-domain access to electronic phenomena calls for the temporal confinement of the sculpted waveform to a single cycle or just a few oscillation cycles. Non-repeatable waveforms of light synthesized by superoctave bandwidth are referred to as light transients (Fig. 1(d)). Recent experiments have paved the way towards this goal<sup>48–52</sup> but they have not yet achieved subcycle field measurement nor on-demand tailoring.

The paper is organized as follows: Section I introduces the principles of light field synthesis and enlists the necessary advancements in light technologies that supply the synthesis of light transients. Section II A introduces the light field synthesis principle. Section II B details the properties of the coherent super-octave light source used in the experiments. The technology of the central apparatus of this work—the light field synthesizer—is discussed in Sec. II C. Sections II D–II G present the alignment and metrology techniques that afford systematic characterization of the properties of the synthesizer as well as passive and active interferometric stabilization schemes. Section III A discusses the attosecond metrology apparatus that enables the complete characterization of generated light transients based on the streaking technique.<sup>8,35</sup> Sections III B–III C discuss attosecond sampling and control of the synthesized waveforms. The paper concludes by outlining current and future implications of light field synthesis in modern ultrafast science and technology.

## II. ELEMENTS OF LIGHT FIELD SYNTHESIS

### A. Light synthesis principles: From femtosecond pulse shaping to subcycle tailoring of light transients

The concept of light field synthesis is schematically illustrated in Fig. 2. Key elements include (i) a coherent light

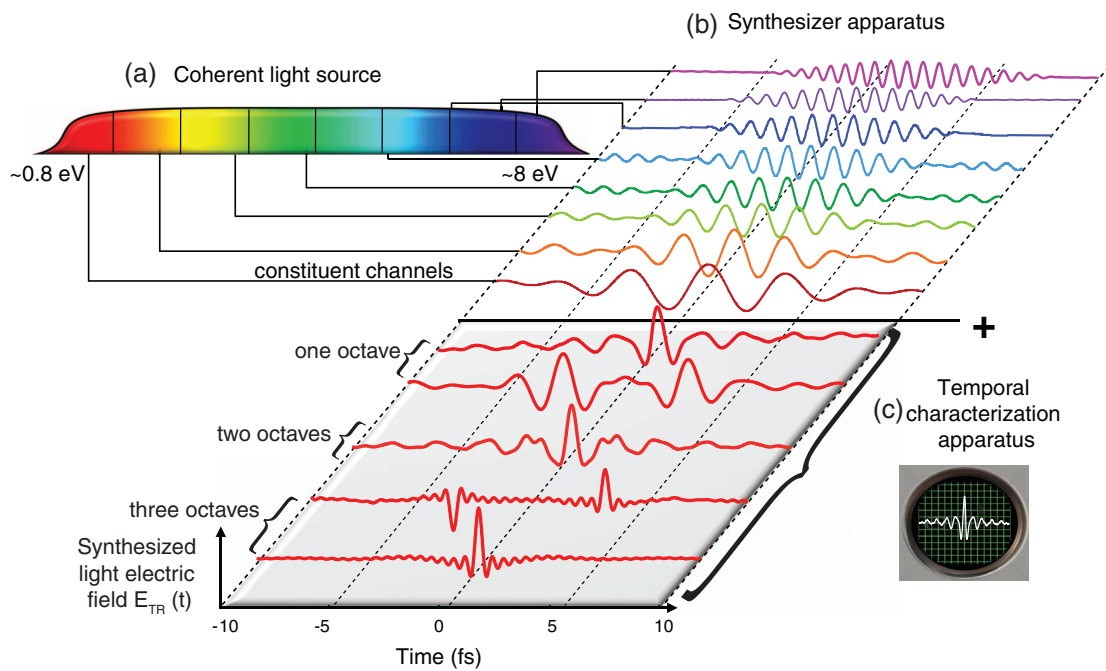


FIG. 2. Principles of light field synthesis. (a) A light synthesizer is used to decompose a broadband light source into its constituent wavepackets. Upon the parallel modulation of their properties such as the relative phase (delay) or intensity the wavepackets are coherently superimposed to create a light waveform at the exit of the synthesizer (b) that can be sampled by an appropriate apparatus (c).

source (ii) a synthesizer apparatus and (iii) a device for temporal characterization of light waveforms. The spectrum of broadband pulses  $\tilde{E}(\omega)$  emerging from the source is decomposed by the synthesizer apparatus into several—spectrally narrower—optical wavepackets  $\tilde{E}_n(\omega)$ , each of them of a width  $\Delta\omega_n$  carried at a central frequency  $\omega_n$ . A light waveform of a prescribed field structure can be synthesized by the coherent spatial and temporal superposition of these wavepackets, following the parallel adjustment of their properties, such as their relative phases, field intensities, or polarization vectors. Since we achieve time-domain control via the manipulation of properties of  $(\Delta\omega > \omega_0)$  a light waveform in the spectral (Fourier) domain, the approach is also referred to as Fourier synthesis. According to the mathematical principles of Fourier synthesis, essential parameters pertaining to, and characterizing a synthesized waveform are the temporal resolution and the time aperture.<sup>11</sup>

The first refers to the shortest temporal feature  $\delta t$  that can be sculpted upon the light waveform. This resolution is simply inversely proportional to the total bandwidth  $\Delta\omega$  occupied by the spectrum:  $\delta t = 2\pi/\Delta\omega$ . Now if  $\Delta\omega$  is comparable to the central (centroid) frequency  $\omega_0$ , the envelope may vary significantly during a single field cycle, giving rise to the possibility of tailoring the sub-cycle structure of the waveform.  $\phi_{CE}$  controlled light pulses briefly mentioned in the previous paragraphs are some of the most prominent manifestations of this capability. For coherent sources having spectra of superoctave bandwidth and are substantially broader than their centroid frequency  $\omega_0$  the field waveform can be sculpted with a precision that is nearing a half-field cycle. This is implying attosecond resolution if the source is centered on the visible part of the spectrum and/or its flanking ranges. The second parameter is the so called “time aperture”  $T$  which describes

the temporal window within which control of the properties of a light waveform can be exercised by a synthesizer,  $T$  is proportional to the inverse bandwidth  $\Delta\omega_n$  of a single constituent channel  $E_n(\omega)$ .

Light synthesis is experimentally complete with the characterization of the temporal profile of the generated waveform at the exit of the synthesizer or, preferably, in the experimental apparatus in which the waveform is being used for studies. The retrieved information can be, in turn, used as a reference for on-demand tailoring of a subsequent light waveform by the synthesizer. In the superoctave realm of light control, it is often questioned if quantities normally used to characterize ultrashort pulses, such as the pulse cycle-averaged envelope or the carrier frequency  $\omega_0$  (here, the centroid frequency), are meaningful at all. They certainly preserve their mathematical rigor, as these are quantities that can be derived for any analytical signal. However, they are in fact less useful in describing the entire set of properties of the field-sculpted light waveforms. In this article, we will nonetheless occasionally use these conventional quantities in order to facilitate comparison of the presented developments with previous efforts in the field of ultrafast science. However, note that the light transients will be best described by their directly measured electric field in any case.

Now, what are the appropriate methods for generating ultrawideband pulses, spectrally dividing them to their constituent wavepackets, manipulating their properties, coherently superimposing them and last but not least, completing the synthesis by temporally characterizing the crafted waveform at the exit of the apparatus? There may not necessarily exist a generic answer to this broad question. The choice of these methods is actually dictated by the envisaged applications which are intrinsically linked to the

TABLE I. Properties/capabilities of light waveforms in the pulse shaping and field synthesis realms of light control.

| Properties                                | Pulse shaping                        | Field synthesis                |
|---|--------------------------------------|--------------------------------|
| Representative microscopic scale of study | Atomic time scale                    | Electronic time scale          |
| Spectral bandwidth                        | <1 optical octave                    | $\geq 1$ optical octave        |
| Temporal resolution                       | Tens of femtoseconds                 | Subfemtosecond                 |
| Field reproducibility                     | No                                   | Yes                            |
| Precision                                 | Femtosecond                          | Attosecond                     |
| Time aperture                             | Picoseconds                          | Femtoseconds                   |
| Dispersion control                        | Generic (prism, grating compressors) | Superoctave dispersion control |
| Power level                               | $\sim$ GW scale                      | $\sim$ PW scale                |
| Light metrology                           | Pulse envelope sensitive             | Field sensitive                |

simultaneous requirements for the resolution  $\delta t$ , the time aperture  $T$ , the strength of the exerted fields, and the complexity of the final waveform. Our efforts in the area of light control are motivated by the desire to trigger, control, and drive the evolution of attosecond/few-femtosecond electron dynamics on the nanometer scale, and thence derive further tools and applications.<sup>53</sup> In order to attain this fine degree of resolution the light waveforms must be tailored with subcycle precision. On the other hand, for this resolution to be effective in experiments, the light pulses must feature the same field waveform (to attosecond precision) from pulse to pulse, and they shall be sufficiently intense to exert forces on valence electrons residing in atoms, molecules, or solids which are commensurable in strength to the forces that keep electrons bounded in these systems.

The above prerequisites can be fulfilled by a significant extension/advancement of the state-of-the-art of modern light technologies. Firstly, the development of coherent, broadband, intense, light sources that span well over super octave bandwidths is essential. This requirement further implies nearly uniform spectral intensities, typically better than  $\sim 30$  dB, to ensure a descent contribution of the weakest spectral components in tailoring the field shape. Whereas this condition is fulfilled by the technique of molecular modulations<sup>42,46</sup> it has been so far possible only for spectra consisting of discrete modes, implying a periodic generation of the light transients which may compromise their usefulness in time-resolved measurements. Secondly, light synthesizers, equipped with the corresponding superoctave spectral response and dispersion control, and exhibiting a high damage threshold of their optical components, must be developed. For instance, a light transient synthesized around the borders of the visible and infrared part of the spectrum ( $\sim 750$  nm) would require optical elements with efficient and damage-free operation from the deep ultraviolet (DUV) to the NIR. In the absence of superoctave pulse compression techniques, dispersion control of the broadband pulses must also be integrated into the synthesizer apparatus. These conditions can hardly be fulfilled by the spectral scaling of pulse shapers. Finally, as the attosecond-scale properties of a waveform and its on-demand synthesis now become central, temporal characterization methods capable of sampling its instantaneous field rather than just its cycle-integrated properties—previously

made possible by techniques like second and/or higher order autocorrelation,<sup>54</sup> frequency-resolved optical gating (FROG), and the spectral shear interferometry for direct electric field reconstruction (SPIDER) technique<sup>55–58</sup>—are now indispensable. Fortunately, direct field sampling methods are readily available as standard tools in attosecond science and are based on the attosecond streaking approach.<sup>35</sup>

Table I summarizes and compares key properties/capabilities of light waveforms for the pulse shaping and the field synthesis realms of light pulse control. A possibly less demanding aspect in field synthesis of intense light transients for electronic control, to be recognized here, is the time aperture  $T$  or the spectral resolution needed to characterize a transient, at least at a level of first applications. Indeed, as electron dynamics typically evolve within hundreds to few thousands of attoseconds, it is implied that a time aperture  $T$  of a few femtoseconds might already be sufficient for a broad scope of electronic processes to be studied and controlled. For the visible range, such a time aperture is compatible to a subdivision of the bandwidth of the coherent source to only 2–3 spectral channels per optical octave. This condition may not hold however if different types of control involve the manipulation of different types of dynamics (electronic, vibrational, rotation, etc.) at the same time.

Other than illustrating the basic principles of light field synthesis, Fig. 2 outlines current and future generations of light control in relation to the bandwidth under manipulation and highlights subcycle synthesis for one optical octave as well as half-cycle synthesis and attosecond synthesis for two optical octaves and beyond.

## B. Superoctave, intense light source

The importance of intense coherent sources of light in the implementation of field synthesis has been emphasized in Sec. II A. To comply with the stringent requirements imposed in this regard, we have opted to spectrally broaden the intense femtosecond light pulses by having them nonlinearly propagate in a gas-filled hollow-core glass waveguide.<sup>59</sup> This approach comprises one of the most effective ingredients of modern pulse compression strategies. Indeed, intense octave-spanning light supercontinua generated

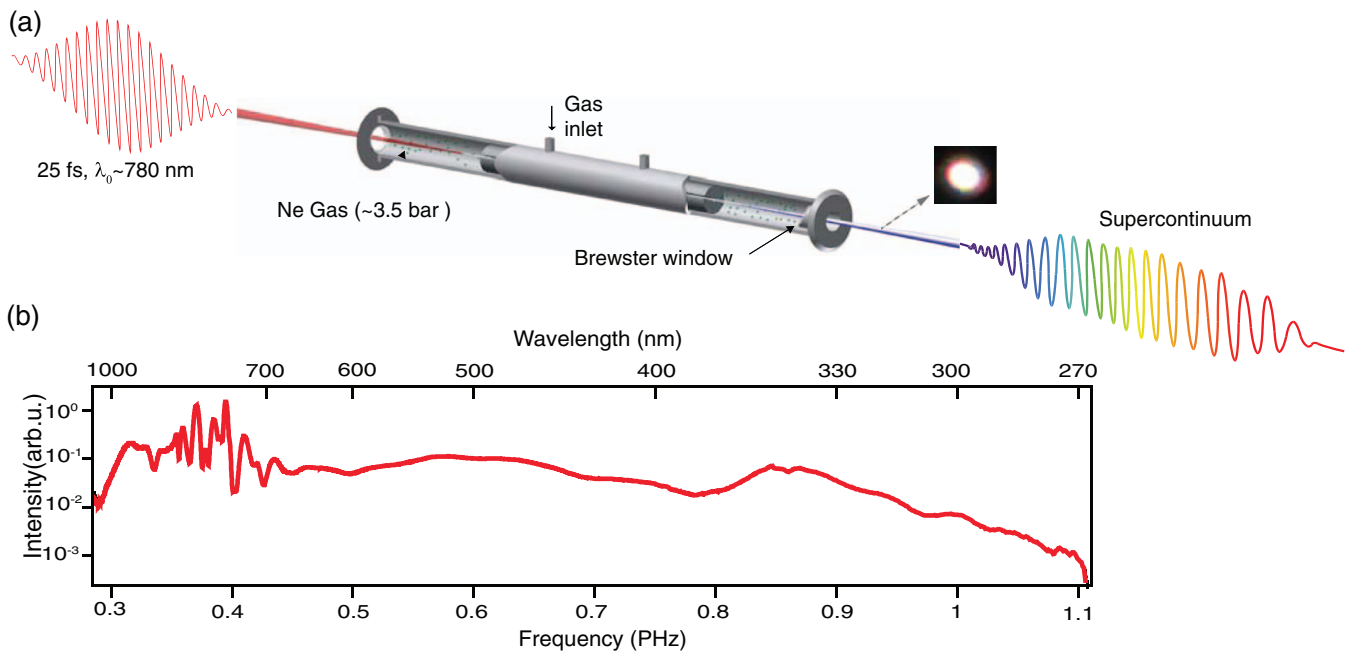


FIG. 3. Superoctave light source in the visible and flanking ranges. (a) Supercontinuum generation in a Ne-filled hollow-core fiber pressurized at  $\sim 3.5$  bar. (b) The generated supercontinuum is spanning over more than two optical octaves ( $\sim 0.8$  PHz or  $\sim 3.3$  eV) with nearly uniform intensity ( $\sim 20$ – $30$  dB). The light beam exits the hollow fiber chamber through a thin UV-grade fused silica window placed at the Brewster's angle to ensure broadband transmission.

with this technique<sup>60,61</sup> and their compression by dispersive mirrors<sup>62,63</sup> has given rise to the generation of pulses with durations down to  $\sim 1.5$  cycles of the carrier wave. In this scheme, the Kerr nonlinearity is the dominant spectral broadening mechanism,<sup>64</sup> responsible for self-phase modulation in the pulse propagating through the gas. Further nonlinear processes,<sup>64</sup> such as shock-front formation<sup>65</sup> across the intensity envelope of the propagating pulse or four-wave-mixing involving remote spectral components in the spectrum of the gradually broadened pulse in the fiber, have also been identified to play a key role in extending the generated supercontinuum to the near and deep ultraviolet at nearly uniform spectral intensities.<sup>66</sup>

In our apparatus, we have implemented the above scheme by focusing ( $f \sim 1.8$  m) pulses produced by a commercial Ti:Sa laser/amplifier system—with a duration of  $\sim 25$  fs, and a pulse energy of  $>800$   $\mu\text{J}$ , a spectral width of  $\sim 70$  nm and a central wavelength of  $\lambda_0 \sim 780$  nm, at the entrance ( $d = 250$   $\mu\text{m}$ ) of a neon-filled hollow core fiber ( $\sim 1.1$  m) mounted inside a capillary. To activate excessive nonlinearity, based on the above mentioned mechanisms, we have adjusted the Ne gas pressure inside the hollow core<sup>67</sup> waveguide to  $\sim 3.0$ – $4.0$  bar. The resulting spectrum spans more than two optical octaves—extending from the IR to the DUV (specifically, from about 1100 nm to 270 nm)—and with nearly uniform intensity ( $\sim 20$  dB), exit the capillary through a thin ( $\sim 0.5$  mm) UV-grade fused silica window which is mounted at Brewster's angle ( $\sim 780$  nm) on the chamber to provide efficient transmission over a broad spectral range. This spectrum is shown in Fig. 3(b). The energy carried by the supercontinuum pulses is  $\sim 450$   $\mu\text{J}$ —implying a  $>56\%$  transmission through the waveguide with an excellent beam profile (Fig. 3(a)) and pulse to pulse energy stability ( $<1\%$  normal-

ized rms). The  $\phi_{CE}$  of the generated supercontinuum pulses is controlled via (i) a fast measurement and control loop (kHz) scheme installed at the exit of the Ti:Sa oscillator<sup>68</sup> as well as by (ii) a second “slow” (tens of Hz) control loop, based on a compact f-2f interferometer<sup>67</sup> placed at the exit of the hollow core fiber to measure and compensate for CE phase drifts accumulated during amplification and/or nonlinear broadening of the pulses. The second f-2f interferometer is seeded by a weak portion ( $<0.2\%$ ) of the generated supercontinuum pulses emerging from the hollow core fiber. The pulse to pulse  $\phi_{CE}$  stability was better than 100 mrad (rms). The divergent beam exiting the capillary is re-collimated to a diameter of  $\sim 9$  mm by a spherical silver-coated mirror ( $f = 87.5$  cm) installed downstream from the source and is guided to the field synthesizer via two additional reflections on flat silver-coated mirrors.

It is important to note at this point that the efficient transportation of the generated superoctave pulses requires optics with high reflectivity/transmission from the UV to the IR. For the experiments presented here, we have opted for silver-coated mirrors as a reasonable compromise between the highly reflective in the NIR for gold-coated and in the DUV for aluminium-coated optics. However, as the technologies presented in this paper are aimed towards ever shorter wavelengths, the challenge of identifying methods of broadband light transportation will need to be addressed with more radical approaches.

### C. Light field synthesizer apparatus

Based on the concepts discussed in Sec. II A, the prototypical light field synthesizer presented here (Fig. 4) and originally proposed in Ref. 54 is based on the broadband

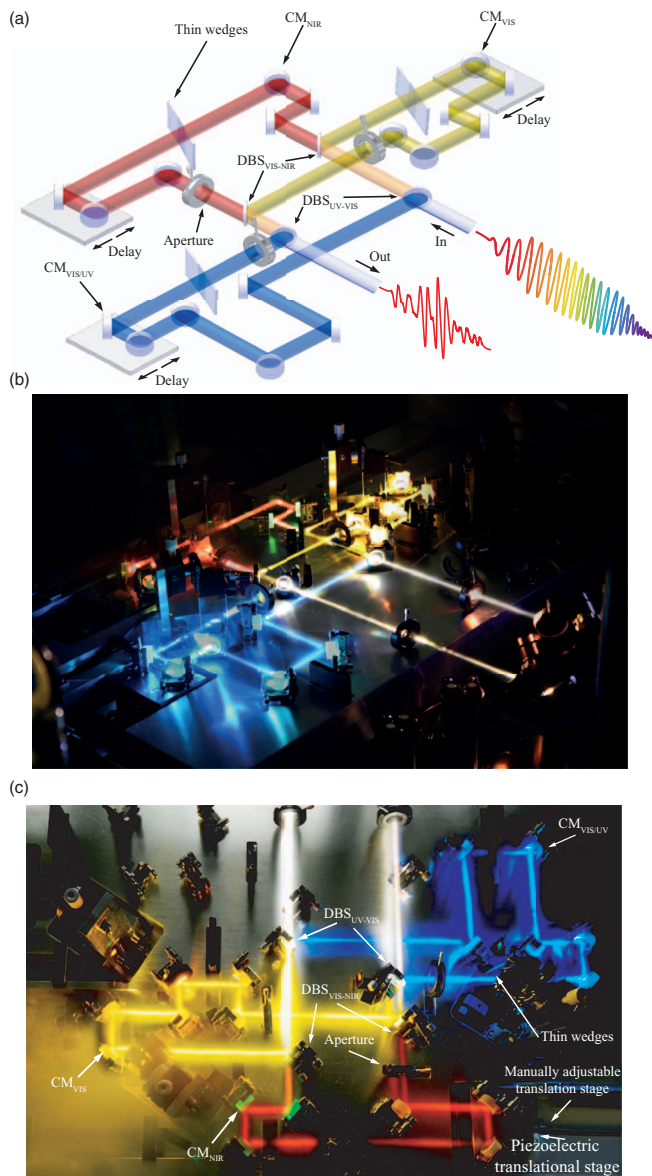


FIG. 4. (a) Schematic representation of a prototypical three-channel super-octave light field synthesizer. DBS, dichroic beamsplitters; CM, chirped mirrors. (b) Photograph (perspective) of the light field synthesizer in operation. (The constituent channels have been visualized by scanning a transparent film through their beams whilst the shutter of the camera is set to an exposure of several seconds.) (c) Top view of the apparatus.

division<sup>53</sup> of the supercontinuum spectra of Fig. 3(b) into three bands (henceforth: constituent channels),  $Ch_{NIR}$  (700–1100 nm),  $Ch_{VIS}$  (500 nm–700 nm), and  $Ch_{VIS-UV}$  (350 nm–500 nm), by custom designed chirped dichroic beamsplitters (DBSs) and their subsequent interferometric spatiotemporal superposition—using the same type of beamsplitters—to synthesize a field waveform at the exit of the apparatus. The theoretical spectral response of the DBS's is detailed in Fig. 5(a). Positive dispersion introduced by the apparatus is minimized by manufacturing dichroic beam splitters on ultrathin fused silica substrates (1 mm or 2 mm) as well as by optimizing the geometrical design of the apparatus so as to reduce the optical path of each channel to  $\sim 54$  cm. The constituent channels of the synthesizer are ordered with respect to the inverse of their

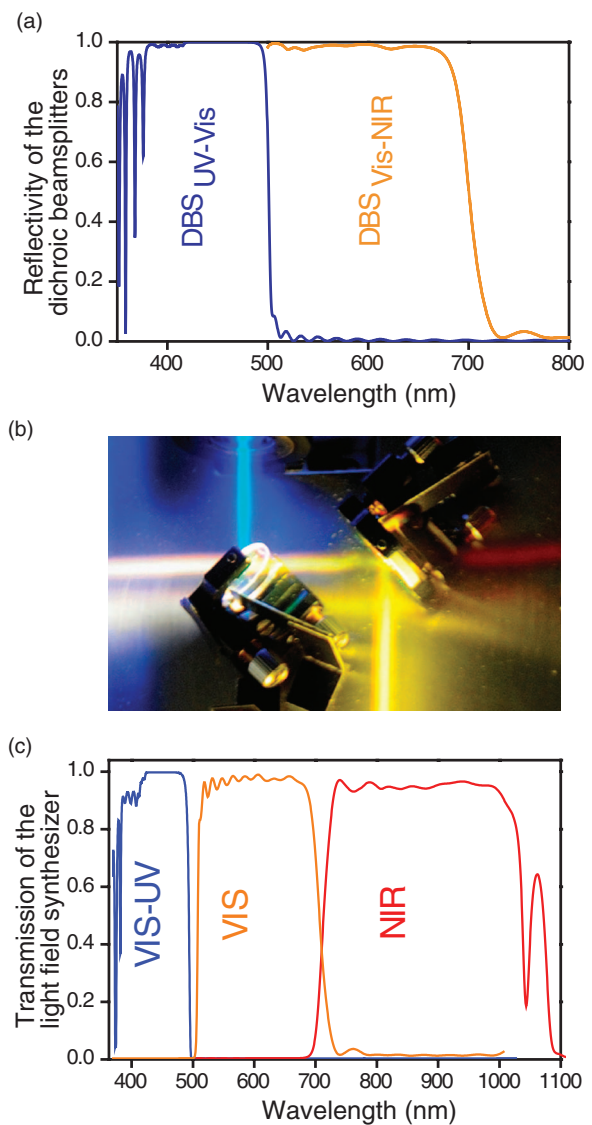


FIG. 5. Dichroic beamsplitters (a) simulated reflectivity of the dichroic beamsplitters (DBS<sub>UV-VIS</sub> and DBS<sub>VIS-NIR</sub>). (b) Photograph of DBS<sub>UV-VIS</sub> and DBS<sub>VIS-NIR</sub> in action. (c) Simulated transmission of the individual channels of the optical field synthesizer. Blue (orange) line includes the reflectivity of two DBS<sub>UV-VIS</sub> (DBS<sub>VIS-NIR</sub>) and six chirped mirrors CM<sub>VIS-UV</sub> (CM<sub>VIS</sub>), whereas the red curve shows the calculated transmission based on six CM<sub>NIR</sub>.

carrier frequency, that is, pulses in  $Ch_{VIS-UV}$  break away from the incoming beam before those of  $Ch_{VIS}$  and pulses in  $Ch_{VIS}$  before those of  $Ch_{NIR}$ . This design strategy is highly important as it minimizes phase distortions of the short wavelength spectral components of the supercontinuum pulses, which are most susceptible to dispersion, while at the same time reducing the complexity (to the benefit of performance) of the DBS's as they must handle narrower spectra as the beam advances into the apparatus. As a case in point, DBS<sub>VIS-NIR</sub> is designed to manipulate a narrower bandwidth as compared to DBS<sub>UV-VIS</sub>. This strategy may also have important consequences for the scalability of the apparatus presented here towards the deep and vacuum ultraviolet in the years to come.

All constituent pulses of the synthesizer are temporally compressed by six dispersive (chirped) mirrors which are introduced into the beam path of the corresponding channel.

These are  $CM_{\text{NIR}}$  for the range (700 nm–1100 nm),  $CM_{\text{VIS}}$  (500 nm–700 nm) and  $CM_{\text{VIS-UV}}$  (350 nm–500 nm). Owing to the considerably reduced spectral bandwidth ( $\sim 1/2$  octave) per channel—as compared to near octave bandwidths which are central in modern developments in dispersive mirrors technology<sup>63</sup>—high reflectivity (Fig. 5(a)) and overall transmission (Fig. 5(c)) through the apparatus are, in principle, attainable as suggested by these theoretical curves. In reality, the contrast of the spectral partition is somewhat lower than designed, especially around the spectral borders of adjacent channels giving rise to a reduced overall transmission through the synthesizer, of the order of  $\sim 83\%$ . The transmission per optical channel is  $Ch_{\text{NIR}} \sim 85\%$ ,  $Ch_{\text{VIS}} \sim 74\%$ , and  $Ch_{\text{VIS-UV}} \sim 57\%$ . The synthesized field transients at the exit of the synthesizer carry an energy of  $\sim 300 \mu\text{J}$  distributed among the three channels as ( $Ch_{\text{NIR}} \sim 250 \mu\text{J}$ ,  $Ch_{\text{VIS}} \sim 36 \mu\text{J}$ , and  $Ch_{\text{VIS-UV}} \sim 14 \mu\text{J}$ ).

A pair of movable, thin, fused silica wedges (apex:  $2^\circ 48'$ ,  $30 \times 20$  mm) introduced in the beam path of the individual channels—at the Brewster angle of each band to ensure minimal losses—are used to fine-tune the dispersion as well as the  $\phi_{\text{CE}}$  of the constituent pulses. In the majority of the planned or already demonstrated<sup>69,70</sup> applications of these technologies, synthesized transients are being formed/used at the focus of a beam, therefore we have opted for control of the relative intensities among constituent channels by the simple introduction of an adjustable iris in the beam path of each channel (Fig. 4(a)). To adjust the relative phase between pulses in different channels, a pair of mirrors in the path of each constituent channel is mounted upon a translation unit comprising (a) a manually adjustable translation stage (precision  $\sim 10 \mu\text{m}$ ) and (b) a piezoelectric translational stage. The first stage permits a coarse adjustment of the optical paths in each channel simultaneously, while finer adjustments of the individual channels with the necessary attosecond precision are enabled by the piezoelectric units. With  $N-1$  channels under optical path control in an  $N$ -channel synthesizer, these degrees of freedom can be completely explored. In the implementation presented here, rough optical path adjustment is possible for all optical channels while fine resolution (via piezoelectric stages) is implemented only for  $Ch_{\text{VIS-UV}}$ , and  $Ch_{\text{NIR}}$ .

#### D. Temporal characterization and compression of pulses in the constituent channels

For the temporal characterization of the pulses in individual  $Ch_{\text{VIS-UV}}$ ,  $Ch_{\text{VIS}}$ , and  $Ch_{\text{NIR}}$ , a compact, transient grating (TG) based FROG apparatus<sup>69</sup> has been employed. In the transient grating beam geometry, signal pulses are generated at the same wavelength range as the pulses under characterization, and therefore it is a highly suitable geometry for the development of a generic characterization apparatus, operating equally well in the infrared, the visible and the deep ultraviolet part of the spectrum. This capability is essential here as pulses in all channels can be characterized without any modification or replacement of the measuring device. To minimize additional dispersion introduced in the device, we have opted for an all-reflective implementation of the TG concept. The device is schematically illustrated in Fig. 8(a) as it has been

additionally used here as a tool for the temporal synchronization of the constituent channels. More details can be found in a previous work<sup>61</sup> where a variation (self-diffraction instead of transient grating) of the apparatus has been used for the characterization of few-cycle pulses in the deep ultraviolet.<sup>61</sup>

For their optimal temporal compression, the spectral phases of the pulses in each channel have been retrieved by FROG measurements (Fig. 6(b)). The measurements are performed initially in the absence of dispersive mirrors. Instead, silver or aluminum mirrors are installed in their dedicated positions. In a next step, the retrieved spectral phases are used as a target for the design of the dispersive mirrors<sup>70</sup> of each channel. To allow flexible dispersion control, we have opted for dispersive mirror designs capable of dealing with the spectral phase introduced to all pulses by roughly  $\sim 4$  m of air plus 3–4 mm of fused silica. Such an optical propagation has required the realization of dispersive mirrors that are able to compensate approximately  $-75 \text{ fs}^2$  per reflection for the chirped mirrors of  $Ch_{\text{VIS-UV}}$ ,  $-70 \text{ fs}^2$  for  $Ch_{\text{VIS}}$ , and  $-70 \text{ fs}^2$  for  $Ch_{\text{NIR}}$ . A more detailed account on the details of the optical coatings and their characterization is out of the scope of this presentation and is detailed elsewhere.<sup>71</sup> With the dispersion in each channel optimized, FROG spectrograms recorded at the exit of the apparatus, and the corresponding, retrieved temporal intensity profiles and phases of the  $Ch_{\text{NIR}}$ ,  $Ch_{\text{VIS}}$  and  $Ch_{\text{VIS-UV}}$  pulses are given in Fig. 6(c). The FWHM of their temporal intensity profile measurement of individual channels are  $\tau_{Ch(\text{NIR})} = 7.9 \text{ fs}$ ,  $\tau_{Ch(\text{VIS})} = 5.5 \text{ fs}$ , and  $\tau_{Ch(\text{VIS-UV})} = 5.5 \text{ fs}$ . These agree well with the bandwidth-limited durations of  $\tau_{Ch(\text{NIR})} = 6.8 \text{ fs}$ ,  $\tau_{Ch(\text{VIS})} = 5 \text{ fs}$ , and  $\tau_{Ch(\text{VIS-UV})} = 4.5 \text{ fs}$ .

#### E. Spatial and temporal superposition of the constituent fields

Synthesis of light fields based upon the coherent superposition of polychromatic pulses calls for a precise spatial and temporal overlap between these pulses. Wavefront matching of the pulses at any point along the propagation axis requires their beams to have the same divergence. This is hardly possible if their beams are transmitted or reflected by various different optical elements which can arbitrarily affect their wavefront, such as beamsplitters, mirrors, thin wedges etc. In particular, deformations induced by the coating strain of the dichroic beamsplitters can severely affect the beam properties. To put this into perspective, for the dichroic beamsplitters employed in our apparatus, a radius of curvature  $f \sim -10$  m is typically induced by the deposition of the dielectric coatings. To mitigate the effect of these deformations, broadband antireflection coatings—deposited at the rear side of each beamsplitter in order to minimize the losses of the transmitted pulses—are optimized to thicknesses comparable to that of the dielectric coating,  $\text{DBS}_{\text{UV-VIS}}$  ( $4.4 \mu\text{m}$ ) and  $\text{DBS}_{\text{VIS-NIR}}$  ( $4.7 \mu\text{m}$ ), which is deposited at the front side. This procedure creates a balance between the strain forces exerted at both faces of the dichroic mirror and results in a rough correction of the deformation. For finer adjustments, a more elaborate scheme has been implemented. It is based on the mechanical adjustment/adaptation of the radius of curvature of a thin (originally flat) mirror installed in the beam path of the

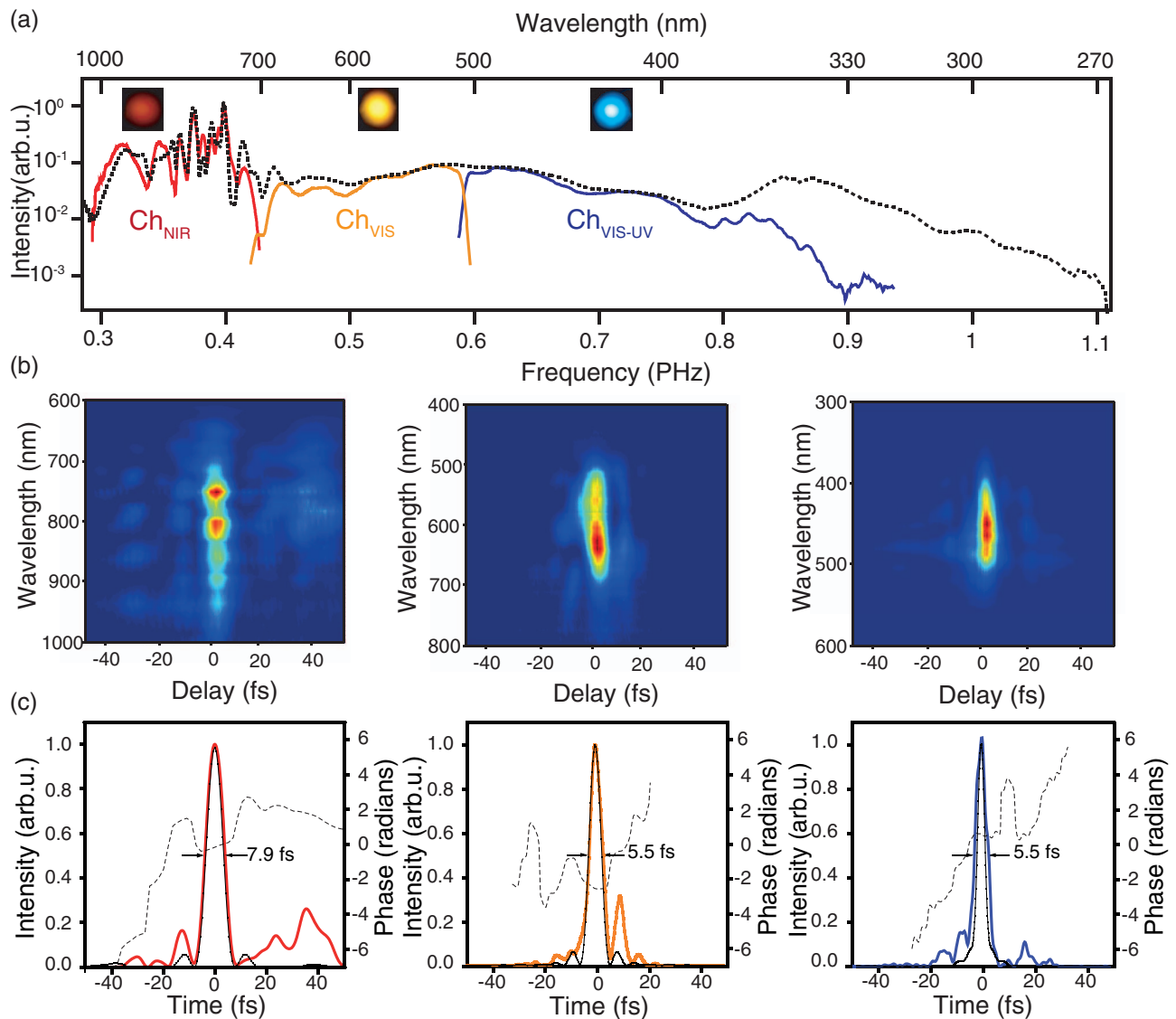


FIG. 6. (a) Spectra of pulses in the constituent channels of the synthesizer are shown in red for  $\text{Ch}_{\text{NIR}}$  (700 nm to 1100 nm), yellow for  $\text{Ch}_{\text{VIS}}$  (500 nm to 700 nm), and blue for  $\text{Ch}_{\text{VIS-UV}}$  (350 nm to 500 nm). The black line corresponds to the spectrum shown in Fig. 3(b). Here it is shown for comparison. Insets show photographs of the beam profiles of the individual channels taken at the exit of the apparatus. (b) TG-FROG traces recorded for the  $\text{Ch}_{\text{NIR}}$ ,  $\text{Ch}_{\text{VIS}}$ , and  $\text{Ch}_{\text{VIS-UV}}$  pulses, respectively and (c) the retrieved temporal intensity (solid lines) and phase (dashed curves) profiles of the respective pulses. The thin black lines depict the intensity profiles of the corresponding bandwidth-limited pulses, with FWHM durations of  $\tau_{\text{Ch}(\text{NIR})} = 6.8$  fs,  $\tau_{\text{Ch}(\text{VIS})} = 5$  fs, and  $\tau_{\text{Ch}(\text{VIS-UV})} = 4.5$  fs.

constituent channels (Fig. 7). The adjustment module (Fig. 7(c)) is based on the action of a micrometric actuator attached upon the rear side of the mirror. Adjustment of the divergence of a beam, within this scheme, results in a displacement of the focal point (here, the center of the confocal parameter) along the propagation axis.

The previous discussion pinpoints the importance of gaining access into the spatial properties of the constituent beams at the exit of the apparatus. As a vast majority of applications will employ focusing of the light transients in order to attain high intensities, it is particularly interesting to explore their spatial properties within the Rayleigh range of the focused beam. To this end, we have installed and used a spherical mirror at the exit of the synthesizer, with a focal length  $f = 40$  cm chosen to simulate the focusing conditions of the beams of the synthesized transients in the experimental apparatus detailed in Sec. III A. In particular, we

have monitored the focal properties of all constituent pulses by a CCD-based beam profiler mounted on a linear motorized stage, translatable along the Rayleigh range of the focused beam. Fig. 7(a) features focal profiles sampled at the beam waist of each constituent channel while Fig. 7(b) shows the variation of the effective beam size (at  $1/e^2$ , averages diameters in  $x$  and in  $y$  axis) along the Rayleigh range. The focal spot sizes of all three constituent beams are quite comparable ( $a_{\text{Ch}_{\text{VIS-UV}}} = 60 \mu\text{m}$ ,  $a_{\text{Ch}_{\text{VIS}}} = 75 \mu\text{m}$ ,  $a_{\text{Ch}_{\text{NIR}}} = 65 \mu\text{m}$ ) primarily due to presence of aberrations on the beams of  $\text{Ch}_{\text{VIS-UV}}$  and  $\text{Ch}_{\text{VIS}}$ , which are reflected off two dichroic beamsplitters each. The spatial profile of  $\text{Ch}_{\text{NIR}}$  is virtually unaffected as the beam path in this channel is comprised only of dispersive mirrors. Most importantly, a considerable longitudinal displacement of the focal spot of  $\text{Ch}_{\text{VIS}}$  suggests aberrations not corrected by the balancing antireflection coating. Corrections implemented by the adjustment of the beam divergence of

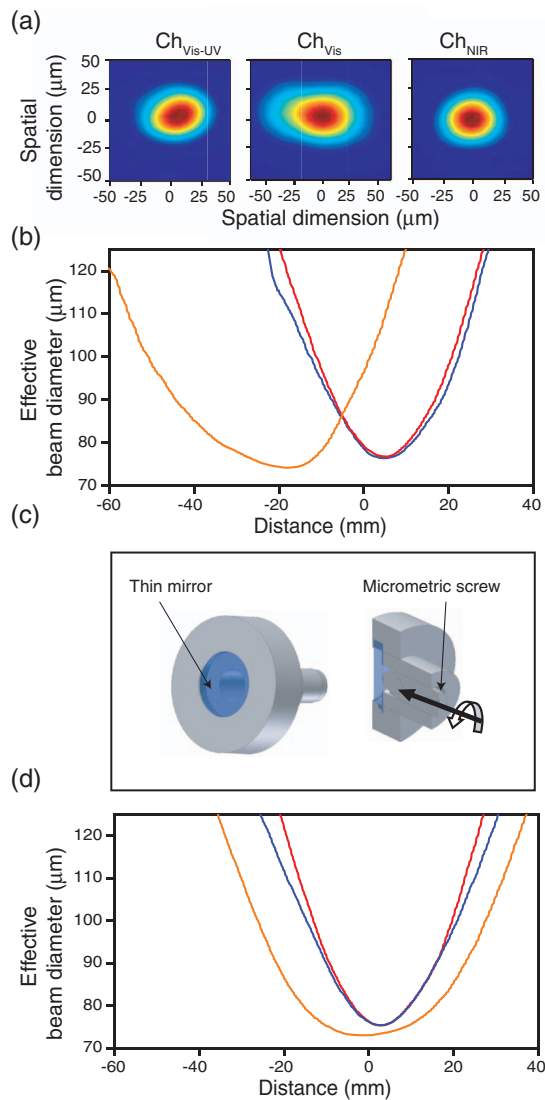


FIG. 7. Spatial superposition of the constituent beams in the field synthesizer (a) beam profiles for pulses in  $Ch_{VIS-UV}$ ,  $Ch_{VIS}$ , and  $Ch_{NIR}$  in the focus of a ( $f = 40$  cm) spherical mirror placed at the exit of the apparatus. The corresponding effective beam diameters are: ( $Ch_{VIS-UV} = 60 \mu\text{m}$ ,  $Ch_{VIS} = 75 \mu\text{m}$ ,  $Ch_{NIR} = 65 \mu\text{m}$ ) (b) Tracing the focal profile of  $Ch_{NIR}$  (red line),  $Ch_{VIS}$  (orange line), and  $Ch_{VIS-UV}$  (blue line) by sampling their beam sizes through their confocal parameters. (c) Module for beam divergence control based on the adjustment of the curvature of a thin mirror installed in the beam path of  $Ch_{VIS}$ . The micrometric screw has a resolution of  $300 \mu\text{m}/\text{revolution}$ . (d) Focal profiles of the beams of the three channels after optimizing the divergence of  $Ch_{VIS}$  with the module presented in (c).

$Ch_{VIS}$  by our module are shown in Fig. 7(d) and yield satisfactory overlap of the foci.

The same experimental setup is also being used for the accurate lateral and angular alignment between beams of the constituent channels. Their overlap in the focal plane ensures their angular alignment whereas the lateral alignment can be achieved by their spatial superposition at the exit aperture of the synthesizer.

## F. Temporal synchronization

For the rough temporal synchronization of the constituent pulses in the light field synthesizer, we have utilized the

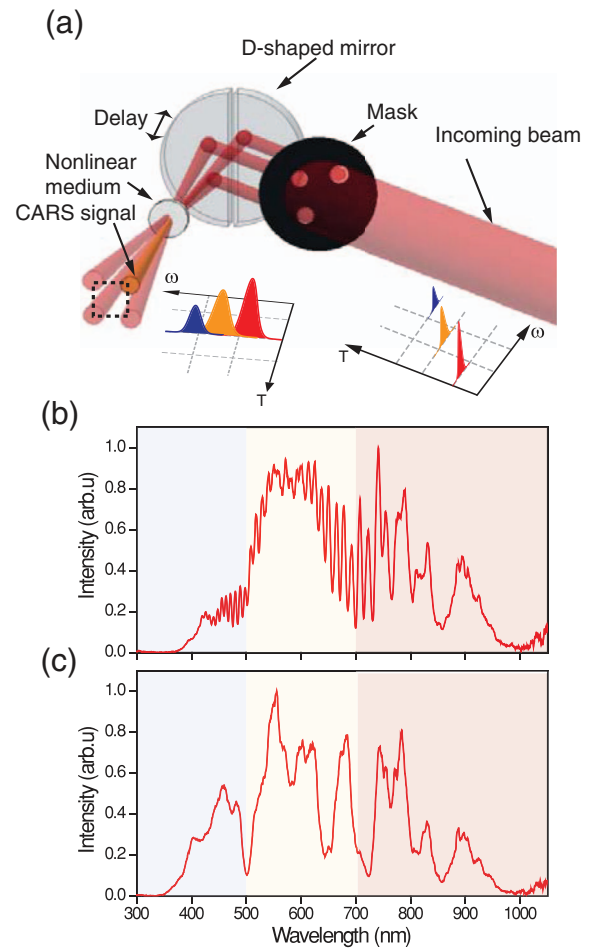


FIG. 8. Temporal synchronization of the constituent channels in the field synthesizer. (a) Schematic of the transient grating FROG apparatus. The input beam is divided into three identical beams via a spatial input mask. The three beams are in turn focused by a split concave mirror to a thin ( $\sim 100 \mu\text{m}$ ) fused silica crystal that acts as the nonlinear medium. A piezoelectric actuator attached on one of the two D-shaped segments of the split mirror is used to introduce a delay with nanometric precision. The  $\chi^{(3)}$  nonlinearity of the process yields signal pulses considerably broader in comparison to the original pulses and results in spectral fringes at the spectral borders of adjacent channels and reveals a delay of several tens of femtoseconds between these channels (b) or temporal overlap to yield a single spectral fringe upon adjustment of the optical paths (c).

transient grating FROG apparatus introduced in Sec. II D, but with a different functionality. In particular, we have exploited the third order  $\chi^{(3)}$  nonlinearity of the transient grating scheme (Fig. 8(a)) to derive signal pulses by each constituent channel, which are spectrally broader as compared to their driver pulse. Hence, although the spectra of the pulses in these channels virtually do not overlap, see, for example, the spectral partitions in Fig. 6(a), interference between their considerably broader nonlinear signal pulses offers a convenient way to trace their relative delays via the principles of spectral interferometry as illustrated in Fig. 8(b), and to adjust it close to zero—yielding a reduced number of spectral fringes or a single fringe as shown in Fig. 8(c).

## G. Passive and active path-length stabilization

In order to ensure long-term stability and reproducibility of the properties of the synthesized light transient—of

paramount importance for its reliable application to high precision attosecond and high field experiments—we have opted for both passive as well as active path length stabilization for the synthesizer apparatus. The three-arm interferometer of Fig. 4(a) has been realized as a quasi-monolithic setup in which the mounts that host the optical components are directly attached to a thermally stabilized, casted aluminum baseplate enclosed into an aluminum housing that protects the optical setup against air fluctuations. Thermal stabilization is achieved by water flow through the volume of the baseplate. The temperature of the water is stabilized at 19 °C by a water cooler with an accuracy of  $\sim 0.1$  °C.

In order to ensure robustness against long term drifts (which are not compensated for by the passive stabilization), an active stabilization scheme has been additionally implemented. This scheme exploits two key features of the experimental apparatus: (a) the superoctave source suffers a small degree ( $\sim 1\%$ – $2\%$ ) of de-polarization, giving rise to *S* polarized components despite that the superoctave source is optimized for *P* polarization, and (b) that each constituent channel in the synthesizer exhibits a wider spectral transmission for its *S* rather than for its *P* polarization components, although at very limited efficiency and dispersion control. These features enable, respectively, (a) the spectral overlap between *S* and *P* polarized spectral components from a channel and its adjacent ones, and (b) the introduction of additional group delay (typically tens to hundreds of femtosecond here) between them, given that the phase properties for *S* and *P* polarization are different in dielectric optics at non-normal incidence. For the use of spectral interferometry as a method to trace and control the timing between pulses in adjacent channels, the latter is essential because it permits the generation of several fringes in the area of spectra overlap between these bands even though the *P* components are perfectly synchronized. Such a delay can be introduced alternatively by calcite plates.

To detect spectral interference and to trace the relative delay between the pulses in different channels, a thin pellicle is used to route a small fraction ( $\sim 2.5\%$ ) of the broadband beam—through a Glan-Thomson polarizer—to the entrance of a fiber spectrometer (Fig. 9(a)). Because the Glan-Thomson polarizer projects *S*-polarized and *P*-polarized components of adjacent channels on the same axis, and adjusts their relative amplitude depending on its angle, it can enable their spectral interference. Spectral fringes recorded between pulses of  $Ch_{VIS-UV}$  and  $Ch_{VIS}$  as well as  $Ch_{VIS}$  and  $Ch_{NIR}$  are shown in Fig. 9(b). Once the two beams are brought to interference, spectral interferometry can be used to derive the relative delays between pulses in adjacent channels.

In order to compensate for the detected drifts in the optical paths among different channels, a computer program is used to analyze the recorded spectra in real-time, such as those of Fig. 9(b), and to accordingly adjust the position of the piezoelectric translational stage in each channel such as to stabilize their relative optical length. Phase drifts between pulses in  $Ch_{VIS-UV}$  and  $Ch_{VIS}$ , as well as between pulses in  $Ch_{VIS}$  and  $Ch_{NIR}$  are shown in Fig. 9(c) over a period of  $\sim 1$  h. The standard deviation of the phase drift between  $Ch_{VIS-UV}$  and  $Ch_{VIS}$  is  $\sim \pi/30$  and that between  $Ch_{VIS}$  and  $Ch_{NIR}$  is  $\sim \pi/60$ . Thanks to the efficiency of the passive stabilization scheme referred

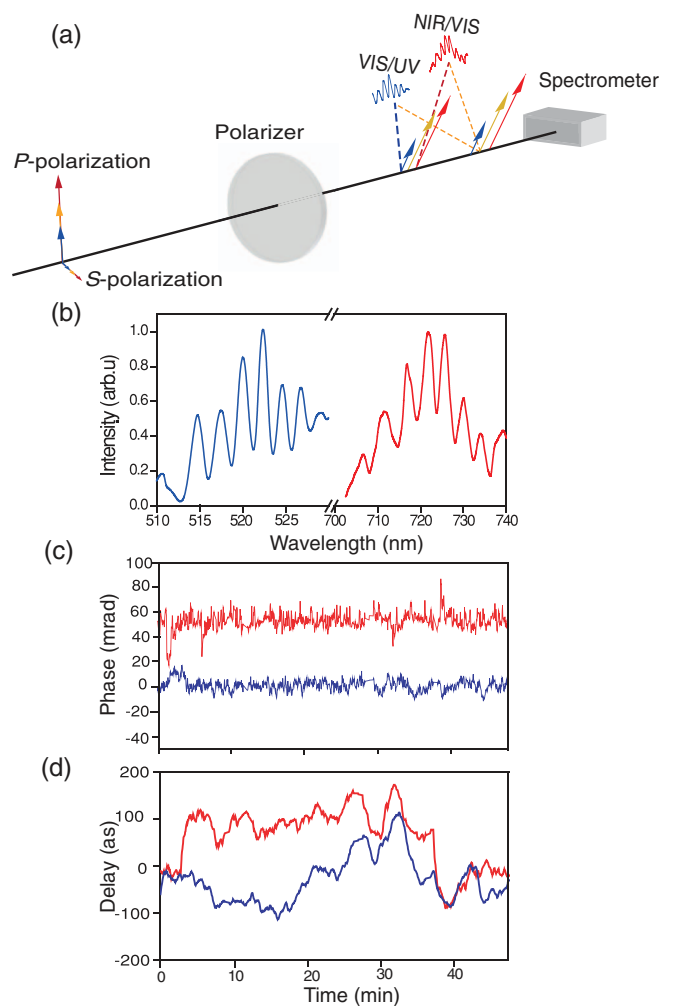


FIG. 9. Active interferometric stabilization of the light field synthesizer. (a) A Glan-Thomson polarizer projects *P* and *S* polarized spectral components from adjacent channels on a common axis to generate spectral interference fringes recorded by the fiber spectrometer. (b) Interference fringes between channels  $Ch_{VIS-UV}$  and  $Ch_{VIS}$  (blue line) as well as  $Ch_{VIS}$  and  $Ch_{NIR}$  (red line) when the constituent pulses of the synthesizer are temporally overlapped at the exit of the synthesizer. (c) Phase drift between ( $Ch_{VIS-UV}$  and  $Ch_{VIS}$ ) and ( $Ch_{VIS}$  and  $Ch_{NIR}$ ) with the feedback loop turned on. The standard deviation of the phase drift between  $Ch_{VIS-UV}$  and  $Ch_{VIS}$  is  $\sim \pi/30$  and  $Ch_{VIS}$  and  $Ch_{NIR}$  is  $\sim \pi/60$ . (d) Corresponding delay compensated for in  $Ch_{VIS-UV}$  and  $Ch_{NIR}$  to yield the results of (c).

to earlier, the active stabilization module is expected to correct drifts at mHz rates only—i.e., delay adjustments once every few seconds. These are typically sufficient to attain long-term stability over a couple of hours, rendering the execution of complex high precision experiments feasible. Fig. 9(d) indicates the adjustment of the optical path in attoseconds for  $Ch_{VIS-UV}$  and  $Ch_{NIR}$ . The nearly random variation of the optical path pinpoints the importance of active stabilization for the long term operation of the apparatus.

### III. COMPLETING THE SYNTHESIS: MEASUREMENT AND CONTROL OF LIGHT TRANSIENTS

Subcycle light transients constitute ideal tools for exploring field-driven nonlinear optical and electronic phenomena but, as alluded to earlier, their synthesis necessitates

direct field characterization of their waveforms. Furthermore, the spatiotemporal transformations of light fields propagating through dispersive media and/or wavefront shaping elements, such as focusing mirrors or apertures, render their properties unique at each point along their propagation axis. Such transformations have a considerably high impact on super-octave light transients. To give an idea of the fragility of these waveforms, a propagation length of 10 cm in air is sufficient to induce a relative delay of  $\sim 7$  fs between pulses in  $\text{Ch}_{\text{VIS-UV}}$  and  $\text{Ch}_{\text{NIR}}$ . Understandably, such a delay of the order of magnitude of the pulse duration greatly affects the temporal profile of these transients. Even in lieu of dispersive elements, for instance, in experiments taking place in vacuum, focusing a polychromatic field will still result in complex spatiotemporal transformations of the waveform due to the frequency dependence of the Gouy phase or more general diffractive effects. In view of these considerations, any robust field characterization needs to take place at the exact point where a light transient is to be exploited in experiments.

### A. Attosecond streaking

For the complete characterization of light transients generated by our field synthesizer, we have opted to use attosecond streaking.<sup>8,35,38</sup> This technique bears close analogy to electro optical sampling used to trace THz transients,<sup>72</sup> and it is based on the employment of a short extreme ultraviolet (EUV) attosecond pulse as a probe to sample the electric field of a light wave. At the same time, as optical fields evolve on a sub-fs time scale, the technique offers the potential of gaining access to the temporal structure of the attosecond pulse. Here, we give a brief introduction to the principles of the technique and in particular its field sampling perspective, as it is critically important for completing light field synthesis. The basic idea employed by attosecond streaking for probing the instantaneous value of a temporally varying field  $E_{TR}(t)$  is to measure the momentum  $\Delta p(\vec{r}, t_r)$  shift (Fig. 10(a)), imparted to an electron  $e$  released into the field at a location  $\vec{r}$  and time  $t_r$ , which is given by  $\Delta p(\vec{r}, t_r) = -e \int_{t_r}^{\infty} E_{TR}(\vec{r}, t') dt'$  and is directly linked to the instantaneous value of the vector potential of the field  $E_{TR}(\vec{r}, t_r)$ , as  $\Delta p(\vec{r}, t) = -e A_{TR}(\vec{r}, t)$ . This relation implies that recording the momentum change  $\Delta p(\vec{r}, t)$  suffered by electrons that are released at consecutive instances  $t$  permits reconstruction of the temporal profile of  $E_{TR}(\vec{r}, t)$  where  $E_{TR}(\vec{r}, t) = -\partial_t A_{TR}(\vec{r}, t)$ . In attosecond streaking, the above considerations are put into practice by exploiting the photoionization of atoms in the presence of the transient. Single-photon ionization is generated by EUV sub-femtosecond pulses which are focused, along with the light transient to be sampled, into an atomic gas jet. To sample the field of the transients, the delay between the two pulses is varied in steps that are shorter than half of the oscillating period of the highest frequency in the transient, in order to comply with the Nyquist-Shannon sampling theorem. As an attosecond burst has a finite pulse length, electrons are not set free within infinitesimally short time intervals. Instead, their photoemission is spread in time to form a wavepacket. Under certain conditions, e.g., in the absence of atomic resonances,<sup>73</sup>

the temporal profile of the photoelectron wavepacket follows that of the EUV attosecond pulse. If the photoelectron release time interval (sub-fs) is commensurable or preferably shorter than the characteristic time of variation of the light field (for visible light a half oscillation period is  $\sim 1$  fs), the momentum of the released wavepackets, which will undergo shifts that follow the vector potential of the field (as can be inferred from Eq. (1)), will also suffer more complex deformations depending on the temporal structure of the attosecond pulse.<sup>74,75</sup> A series of electron spectra recorded as a function of the delay between the light transient and the attosecond pulse is referred to as a streaking spectrogram. In the years that followed the first demonstration of the concept<sup>5,8,9</sup> and its proliferation to other laboratories,<sup>38,76,77</sup> various techniques have been developed to evaluate streaking spectrograms. Some of the most prominent of these treat the spectrogram with reconstruction algorithms originally developed for FROG.<sup>78</sup> Here, the sub-cycle variation of the light field serves as an attosecond phase gate to capture the transient properties of the photoemission and therewith those of the attosecond pulse.<sup>74,75</sup> Typically, these methods reconstruct the spectrogram based on a numerical algorithm, offering access to both the pulse and the gate. Within the context of attosecond streaking, the former is the attosecond pulse field while the latter contains the field of the light transient.<sup>79</sup> In the experiments presented next, we have explored ATTOGRAM<sup>80</sup> to reconstruct the temporal dynamics of our attosecond pulses. Of course, for the reconstruction of the fields of the synthesized transients only, an application of the FROG method is not necessary. Thus we have opted for a simplified, but equally accurate and more direct method discussed in Sec. III B which offers very prompt access into the field profile of the transient and enables on-demand feedback to the synthesizer.

In our experiments, the setup that incorporates the above ideas is depicted in Fig. 10(b). Light transients generated by our field synthesizer apparatus are focused ( $f \sim 40$  cm) into a quasistatic gas cell filled with Ne ( $p \sim 200$  mbar), yielding a peak intensity of  $I_{TR} \sim 10^{14}$  W/cm<sup>2</sup>. Here, the nonlinear interaction leads to the generation of extreme ultraviolet radiation by means of high-order harmonic generation.<sup>81</sup> The gas cell, as well as the rest of the experimental setup discussed henceforth, is fully realized in vacuum,<sup>67</sup> in which the synthesized transients enter through a 0.5 mm thin UV-grade fused silica Brewster window.

Nearly diffraction-limited EUV pulses emerging collinearly to the driving radiation are transmitted through a disc-like Zirconium (Zr) foil (thickness of  $\sim 150$  nm) mounted on a thin nitrocellulose pellicle ( $\sim 15$   $\mu\text{m}$ ), while the driving radiation, which also travels through the gas cell, is transmitted around the margins of the Zr disc and through the thin pellicle to create an annular beam. A module comprised of a concave multilayer coated inner mirror, and an aluminum coated concave annular sector (outer mirror) of the same focal length ( $f = 12.5$  cm), is used to focus EUV pulses and light transients, respectively, into a second Ne gas to implement the streaking technique. The profiles of the beams of the three channels at the place of characterization are monitored by imaging the focus on a CCD camera through a broadband achromatic lens.

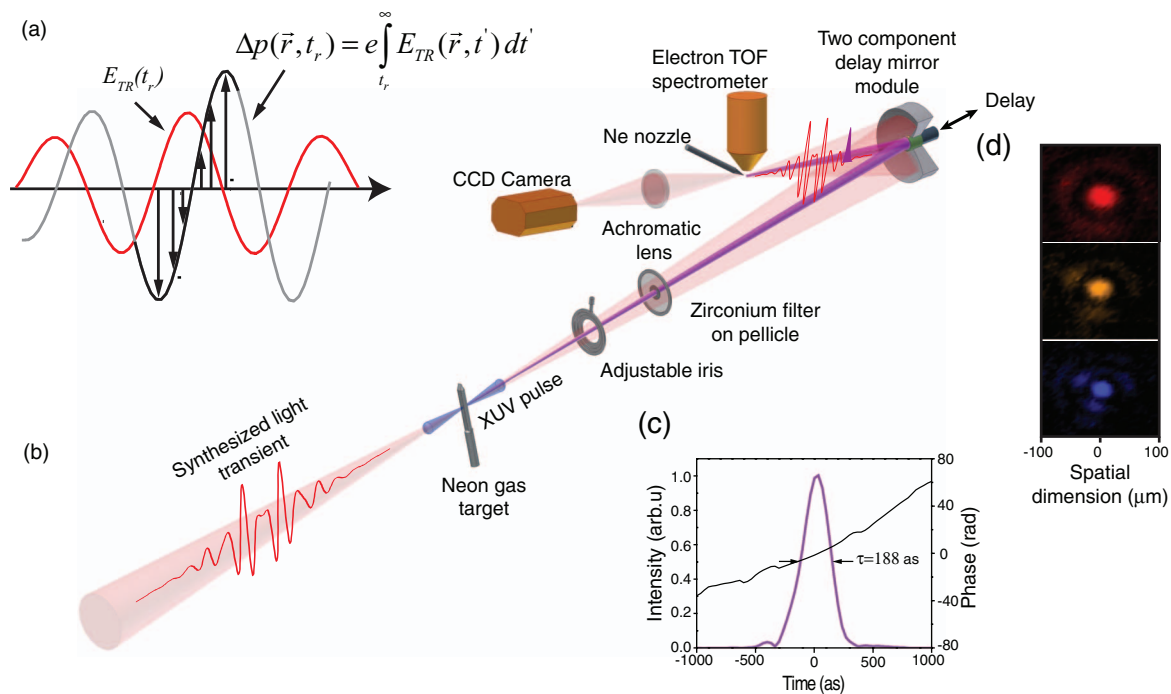


FIG. 10. Attosecond streaking technique and its basic elements. (a) Principles of attosecond light sampling based on the attosecond streaking technique. A synthesized light transient  $E_{TR}(t)$ , along with a synchronized attosecond EUV pulse, is focused into an atomic gas target. The EUV pulse knocks electrons free by photoionization at an instance  $t_r$ . The field of light  $E_{TR}(t > t_r)$  then imparts a momentum change  $\Delta p(\vec{r}, t_r) = e \int_{t_r}^{\infty} E_{TR}(\vec{r}, t') dt'$  to the freed electrons, which scales as the instantaneous value of the vector potential  $A_{TR}(t_r)$  at the moment of release  $t_r$ . The momentum change  $\Delta p(t_r)$  is recorded by an electron time-of-flight detector, placed along the direction of the linearly polarized  $E_{TR}(t)$ . (b) Schematic diagram of the experimental setup for sampling synthesized light field transients (see text for details). (c) Retrieved temporal intensity profile and spectral phase of the EUV pulse. (d) The beam profiles of the constituent channels on the focal plane on which synthesis and temporal characterization of light transients is been performed.

A time of flight electron spectrometer with a spectral resolution finer than 1% of the electron kinetic energy is used to collect electrons released along the EUV pulse polarization vector. The multilayer mirror coating, together with the high pass Zr filter, comprises a band pass filter of width  $\Delta E \sim 13$  eV centered at  $E_0 \sim 82$  eV that lies close to the cutoff energy of the EUV radiation generated at the source  $E_c \sim 95$  eV. The inner mirror is attached to a piezoelectric stage that allows the introduction of a delay between the light field transient and the EUV attosecond pulse with nanometric precision. A controllable iris is used to adjust the energy transported by the beam of the light transient from the level of few microjoules (adequate for streaking) to that of several tens of microjoules for strong field attosecond experiments, offering a dynamic range over several orders of magnitude, from  $<10^{12}$  W/cm<sup>2</sup> to  $\sim 10^{15}$  W/cm<sup>2</sup>.

Streaking measurements are typically performed at  $10^{12}$  W/cm<sup>2</sup> to avoid strong-field ionization of the atom by the transient. Fig. 10(d) shows representative beam profiles of the constituent channels on the focal plane of the double mirror module, on which synthesis and temporal characterization of light transients is performed. A representative temporal profile of an attosecond pulse retrieved from streaking spectrograms that are presented in detail later in this paper reveals a pulse duration of  $\sim 188$  as (Fig. 10(c)). This is substantially shorter than the half-optical cycle corresponding to the highest frequency of our transient

( $\sim 0.6$  fs) and ensures aliasing-free sampling of the field transients.

## B. Retrieval of the field waveforms

As light transients are the centerpiece of this study, we do not require the complex machinery afforded by FROG-type reconstruction algorithms. In order to fully characterize the light transients, a simplified,<sup>82</sup> considerably faster (seconds) and less noise-sensitive, but equally accurate retrieval method is sufficient. This method is based on the evaluation of the first moments (centroids) of the streaked photoelectron spectra as a function of the time delay between the EUV and synthesized transient fields. This approach facilitates real-time retrieval and feedback to the synthesizer apparatus, which is essential for the on-demand synthesis of light fields detailed in Sec. III C. The light transients characterized by this method agree with those of the detailed FROG analysis of the streaking spectrogram. The basic underlying assumption in this approach is that the attosecond pulse is shorter than a half-cycle of the light transient, which is accurate down to wavelengths of  $\sim 120$  nm for the measurements presented here. First, the attosecond EUV pulse can be modeled as:  $E_{EUV}(t) = |E_{EUV}(t)| \exp[i(\omega_{EUV}t + \varphi(t))]$  where  $\omega_{EUV}$  is the central EUV frequency and  $\varphi(t)$  contains higher-order temporal phase variations (chirp). Such an EUV pulse ionizes

the atom, say with ionization energy  $W$ , by launching photoelectron trajectories in a continuum permeated by a laser field at various moments  $t$ . These trajectories end at the detector with a final kinetic energy  $E_K(t)$ , which is given (in atomic units  $\hbar = a_0 = 4\pi\epsilon_0 = m_e = 1$ ) by

$$E_K(t) = \left( \sqrt{E_0 + \dot{\phi}(t)} - \frac{1}{\sqrt{2}} A_{TR}(t) \right)^2 \approx E_0 - p_0 A_{TR}(t) + \frac{1}{2} A_{TR}^2(t) + \left( 1 - \frac{A_{TR}(t)}{p_0} \right) \dot{\phi}(t), \quad (1)$$

with  $p_0 = \sqrt{2E_0}$ , and  $E_0 = \omega_{EUV} - W$ .

Since the variations in the attosecond pulse's instantaneous frequency, represented by  $\dot{\phi}(t)$ , are small compared to its central frequency  $\omega_{EUV}$ , the final term on the rightmost-hand side of Eq. (1) is negligible. This implies that the center of the streaked photoelectron spectrum is insensitive to the phase of the attosecond pulse. Moreover, if the attosecond pulse is shorter than a half-cycle of the laser field, the central energy  $E_S$  of the streaked photoelectron spectrum is well approximated by  $E_S \approx E_K(t_r)$ , where  $t_r$  is the central time of the attosecond pulse. This allows for a direct evaluation of the vector potential  $A_{TR}(t)$ , which in turn yields the complete time dependence of the synthesized waveform's electric field

$$E_{TR}(t) = -\partial_t A_{TR}(t).$$

Details on the numerical implementation of the algorithm are given in Appendix A.

### C. Measurement and on-demand synthesis of field waveforms

In our prototypical scheme presented here, field synthesis and measurement are partially linked, as the EUV attosecond pulses are spawned by the synthesized transient at the first gas jet of Fig. 10(b) before being used to sample its driver field at the second gas nozzle. While the coupling between the transient and attosecond pulse fields is not a necessity—these two processes can, in principle, be separated by a modified experimental arrangement—the current implementation features an important advantage for achieving attosecond timing between the constituent channels of the field synthesizer. In particular, the relative timing of the constituent channels can be adjusted to maximize the EUV emission. To this end, a back-illuminated CCD camera placed downstream from the EUV source is used to record the flux of EUV radiation transmitted through an approximately  $\sim 1 \mu\text{m}$  thick Zr foil. The Zr foil allows the transmission of photons with energies exceeding  $\sim 70$  eV up to the cutoff energy  $E_c$  which was adjusted to approximately 95–100 eV. Fig. 11(a) depicts streaking spectrograms of a field waveform recorded following the adjustment of the relative phases (delays) between pulses in  $\text{Ch}_{\text{NIR}}\text{-Ch}_{\text{VIS}}$  and  $\text{Ch}_{\text{VIS}}\text{-Ch}_{\text{UV-VIS}}$ , respectively, to maximize the EUV photon yield generated in the first gas cell of Fig. 10(b). Each photoelectron spectrum in the spectrogram is integrated over  $\sim 9000$  laser shots while the delay has been varied in steps of  $\tau \sim 200$  as. The effect of shot-to-shot intensity fluctuations (despite at a  $< 1\%$  level), which inevitably

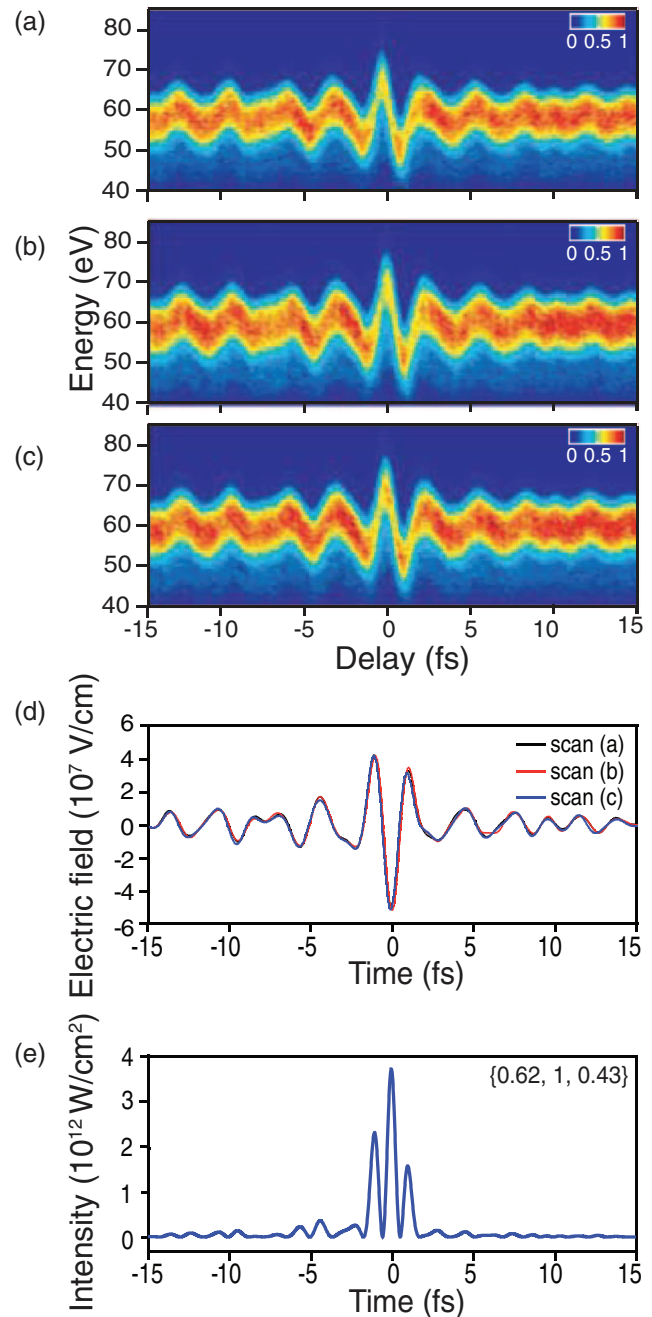


FIG. 11. (a)–(c) Streaking spectrograms of a synthesized light transient sampled sequentially over a period of  $> 1$  h. (d) The corresponding retrieved electric field waveforms in comparison. The rms discrepancy between the sampled field waveforms is less than 0.09, suggesting excellent reproducibility of the synthesized fields. (e) The instantaneous intensity profiles of one of the waveforms shown in (d) further corroborate the extreme temporal confinement of the generated transients. In brackets, instantaneous intensities of the field crests normalized to that of the most intense field crest.

affect the total number of counts per photoelectron spectrum within the  $\sim 3$  s of its acquisition, is eliminated by normalizing each sampled spectrum of the spectrogram to its integral. This procedure allows us to reveal the details of the spectrogram in the false color representation but has no influence on the analysis presented in Sec. III B. Detailed analysis of the attosecond properties of the EUV pulses is, however, performed without this normalization.<sup>34,83</sup> With the relative phases between the constituent channels of the apparatus

locked—based on the methodology discussed in Sec. II G—we recorded a series of streaking spectrograms in order to investigate (i) the stability of the synthesized waveforms over long time periods and (ii) their physical properties. A first spectrogram recorded is shown in Fig. 11(a). Next, the sampling process is repeated twice, yielding the streaking spectrograms shown in Figs. 11(b) and 11(c). The acquisition time for each spectrogram was approximately 20 min, implying a total acquisition time of  $>1$  h. The retrieved field waveforms from the spectrograms in Figs. 11(a)–11(c) are plotted in Fig. 11(d) for comparison. A simple inspection of the recorded traces and their retrieved waveforms affords the conclusion that the synthesized transients retain exceptional stability and reproducibility for long periods. To put this more into perspective, the rms field difference<sup>84</sup> between these transients is only 0.09 on a  $\pm 15$  fs window, which demonstrates the robustness of the technique. This stability is an essential prerequisite both for the detailed study and control of the transients, as well as their reliable use in high precision experiments.

Moreover, Fig. 11(d) reveals fine details of the temporal subcycle evolution of the field waveform and its extreme temporal confinement which can be inferred by the dramatic intensity contrast of 40% (Fig. 11(e)) between adjacent field half-cycles, revealing the subcycle nature of the transient. Similar conclusions can be drawn from the estimation of the fraction of energy of the transient enclosed into single intense field half-cycle, yielding more than 35%.

Each light transient recorded by our apparatus can be used as a reference to access the detailed properties of the field synthesizer at a certain time. These include the pulse properties in each individual channel, and their relative phases (or delays). To evaluate these parameters from a reference waveform, as shown in Fig. 12(b), band-pass filtering constrained to the spectral margins of each channel is performed (Fig. 12(c)). Remarkably, some of the pulse properties of the individual channels extracted via this methodology ( $\tau_{\text{Ch(NIR)}} = 7.3$  fs,  $\tau_{\text{Ch(VIS)}} = 5.5$  fs, and  $\tau_{\text{Ch(VIS-UV)}} = 4.5$  fs) agree well with those retrieved with the FROG measurements presented in Sec. II D. Knowing these parameters, on-demand synthesis of a subsequent waveform can be performed through their appropriate adjustment. As an example, Fig. 12(e) shows a waveform that could be synthesized, on demand, by the adjustment of the relative phases of  $\text{Ch}_{\text{VIS-UV}}$  by  $\pi/2$  and of  $\text{Ch}_{\text{NIR}}$  by  $\sim\pi$ .

Figure 13 demonstrates how these ideas are applied practically for the subcycle control of light transients. The electric fields (red lines, middle column) and instantaneous intensities (right column) are derived from the corresponding streaking spectrograms (left column). The light transient shown in Fig. 13(a) is set here as the reference. Field transients in Figs. 13(b) and 13(c) are synthesized by delaying  $\text{Ch}_{\text{VIS-UV}}$  in steps of  $\pi/4$  ( $\sim 200$  as) with respect to the reference waveform in (a). The field waveform in (d) is generated by delaying  $\text{Ch}_{\text{VIS-UV}}$  by  $-\pi/2$  to reproduce the reference of Fig. 13(a). Black lines in Figs. 13(b) to 13(c) correspond to simulated waveforms calculated by the reference waveform and by delaying  $\text{Ch}_{\text{VIS-UV}}$  by the corresponding amounts as illustrated in Fig. 12, and by translating the time axis as de-

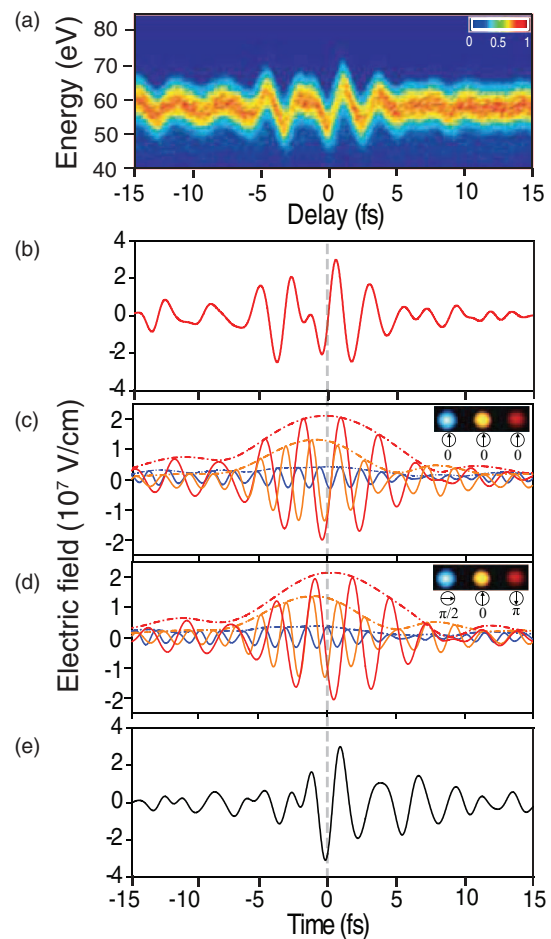


FIG. 12. Designing a light transient. (a) Attosecond streaking spectrogram of a reference transient and (b) its corresponding retrieved field. (c) Decomposition of the retrieved field into its constituent channels reveals their detailed properties including their durations ( $t_1$ ). By the adjustment of the relative phases of  $\text{Ch}_{\text{VIS-UV}}$  by  $\pi/2$  and of  $\text{Ch}_{\text{NIR}}$  by  $\pi$ , the design of a different waveform is possible (d). (e) The corresponding changes in the parameter space can be subsequently applied to the field synthesizer to synthesize the light transients experimentally (cf. Fig. 13).

scribed in Appendix B. Fig. 13(e) shows a substantially more complex, nonsinusoidal transient generated by adjusting the  $\phi_{CE}$  phases of all channels and the delay of  $\text{Ch}_{\text{NIR}}$  such that the fields of the three constituent channels cancel each other at the center of the synthesized waveform. Adjusting the delay of  $\text{Ch}_{\text{NIR}}$  by  $\sim\pi$  results once again in a transient of sub-cycle temporal confinement, in which the field of the most intense field crest is pointing in the opposite direction compared to the transient of Fig. 13(a).

The effect of these transformations on the instantaneous intensity of the synthesized transients is revealed in Fig. 13 (right column). Delaying  $\text{Ch}_{\text{VIS-UV}}$  gradually transforms the field into the highly asymmetric transient of Fig. 13(c), leaving the temporal confinement of the waveform nearly unaffected. The transient is led by its most intense half-cycle, followed by field crests with gradually decreasing intensity—relative intensities normalized to the most intense half cycle are shown in brackets—giving rise to a transient having a leading edge of a sub-fs rise time. The waveform in Fig. 13(e) reveals a transient for which the two most intense field crests

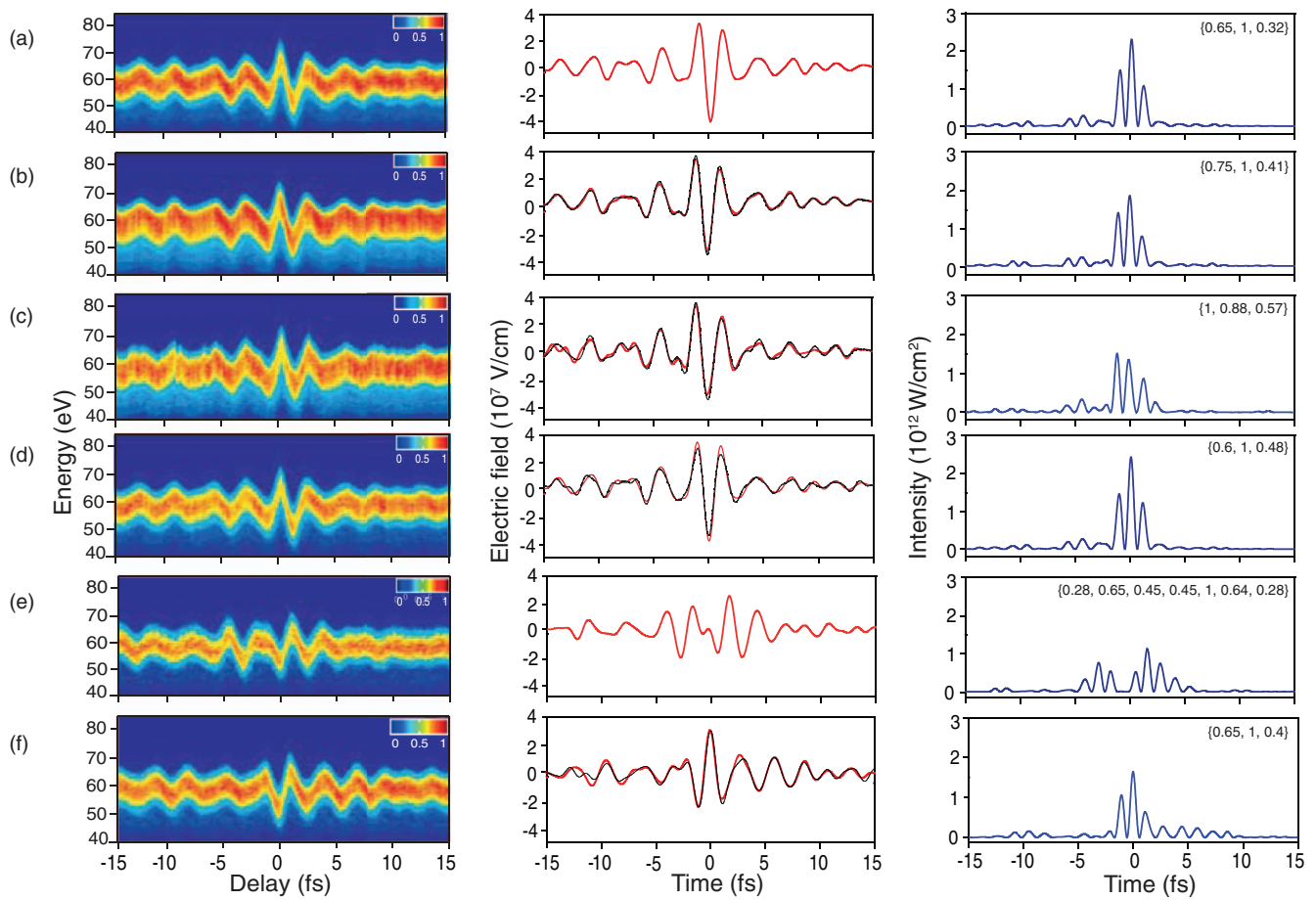


FIG. 13. Subcycle synthesis of light transients and their control. (a) to (d) Attosecond streaking spectrograms composed by photoelectron spectra normalized to their integral (left), the respective retrieved electric fields (red line), and the predicted field transients calculated from the previous light transient by applying the delay introduced experimentally (black line). The predicted theoretical electric fields are in good agreement with the measured electric field (middle) and instantaneous intensity (right). In brackets, instantaneous intensities of the field crests normalized to that of the most intense field crest. From (a) to (b)  $\text{Ch}_{\text{VIS-UV}}$  delayed by 200 as ( $\sim\pi/4$ ) with respect to the  $\text{Ch}_{\text{VIS}}$  and  $\text{Ch}_{\text{NIR}}$ , from (b) to (c)  $\text{Ch}_{\text{VIS-UV}}$  delayed by an additional 200 as ( $\sim\pi/4$ ), from (c) to (d)  $\text{Ch}_{\text{VIS-UV}}$  set to have the same relative delay setting with the other channels as in the original light transient (a). (d) Relative delays and  $\phi_{CE}$ 's of the individual channels are adjusted so as to create a complex nonsinusoidal transient with a field minimum in between them. (e)  $\text{Ch}_{\text{NIR}}$  is delayed by 1.45 fs ( $\sim\pi$ ).

of which are separated by  $\sim 4.5$  fs and a virtually annihilated half cycle in its middle.

Next, we set out to derive a few conventional properties of our light transients that could also facilitate their comparison to other developments in ultrafast science. Based on the methodology discussed in Appendix A, we derive the intensity envelope of the transient shown in Fig. 14(b). The intensity envelope is shown in Fig. 14(c). The analysis yields a FWHM pulse duration of  $\sim 2.08$  fs which constitutes, to our knowledge, the shortest visible light pulse generated to date, based on this broadly accepted definition of pulse duration. The blue line corresponds to the Fourier limited intensity profile. The comparison between the two profiles suggests that a failure to perfectly compress the pulses in the constituent channels of the synthesizer merely affects the temporal confinement of the synthesized light transients; it results in partial energy redistribution into the pedestal of the transient. This fact has important implications for the reproducible generation of subcycle transients on a day-to-day basis, as it suggests that their synthesis will be possible even if the exact conditions—for instance, the compression of the constituent channels—are not perfectly reproduced.

Moreover, this analysis further justifies the term “subcycle,” extensively used for the light transients in this text: The term “subcycle” implies a comparison between a pulse’s width to the period of its carrier wave. Following the analysis of Appendix A, the evaluated, carrier wavelength  $\lambda_c = 710$  nm corresponds to an oscillation period of  $T_c = 2.34$  fs. This is also in good agreement with that estimated by the weighted averaged wavelength derived from the spectrum in Fig. 3(b) which is directly measured at the exit of the synthesizer. Hence, the generated transients encompass only 0.88 cycles within the FWHM of their intensity profile.

#### IV. OUTLOOK

We have presented the technology of what we believe to be a new realm in light control: the synthesis of subcycle transients of the electromagnetic field and the attosecond tailoring of its waveform. Whereas subcycle field synthesis requires the manipulation of coherent, superoctave light sources, its successful implementation is compatible with the subdivision of this bandwidth into a limited number of

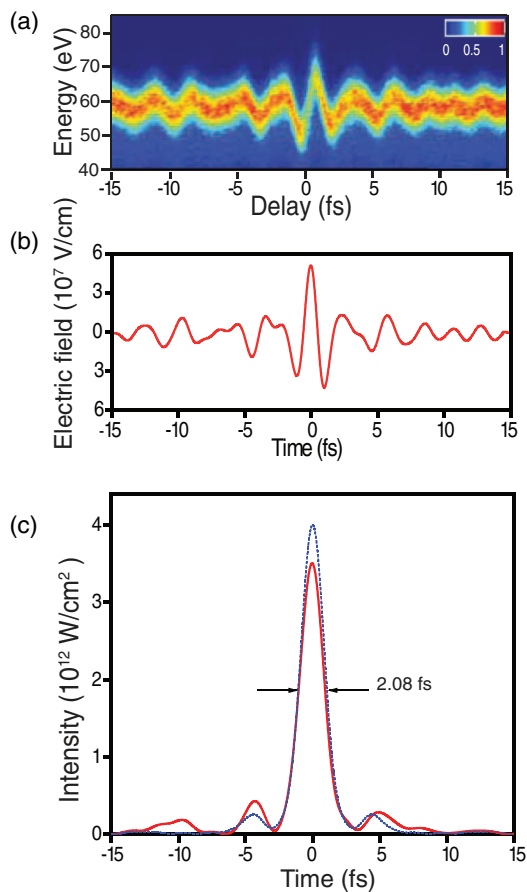


FIG. 14. Light transients under conventional analysis: (a) attosecond streaking spectrogram, (b) the retrieved electric field, and (c) temporal intensity profile (red) of sub-optical cycle pulse with a  $T_{FWHM} \sim 2.08$  fs, incorporating  $\sim 0.88$  field cycles at the carrier wavelength of  $\lambda_0 \sim 710$  nm compared to the bandwidth limited profile (blue).

constituent spectral channels as long as dispersion affective of the pulses in each of these channels is possible. The light field synthesis concepts detailed in this work also affords scalability over several more optical octaves by the introduction of additional spectral channels in the deep and vacuum ultraviolet, as well as in the infrared region of the spectrum, as envisaged in Fig. 2.

Obviously this extension is critically linked to the development of novel and efficient supercontinuum light sources extending into these spectral ranges. The hollow-core fiber based source presented here can support these efforts at least down to the deep ultraviolet, as suggested by the spectra of Fig. 3(b). Moreover, recent progress in the development of superoctave VUV sources<sup>85</sup> promise the extension of these technologies into this demanding, but highly important part of the spectrum. Furthermore, these advances will be supported by the recently established few-cycle pulse metrology in this spectral range,<sup>61,86–88</sup> along with an important role played by the development of light sources in the near and mid-infrared.<sup>89</sup> The simplicity of the light field synthesizer, and the fact that it is based exclusively on dielectric optics affords power scalability by simply increasing the size of the optics in the apparatus to sustain synthesis of pulses in the multiterawatt or pettawatt scales.

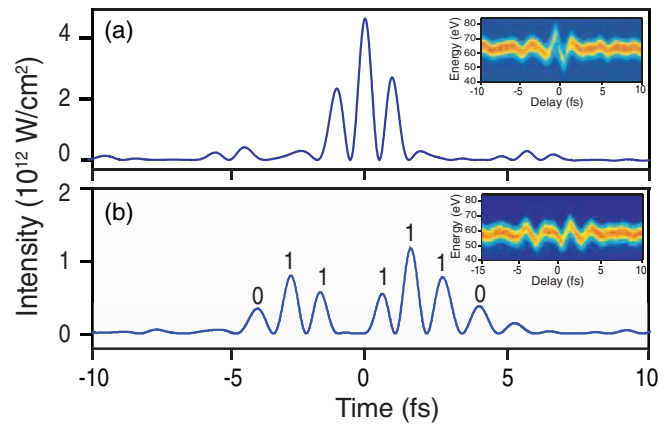


FIG. 15. Instantaneous intensity profile of synthesized light transients appropriate for (a) triggering ultrafast dynamics by strong field ionization of atoms, molecules or solids (b) coherent control of the creation of atomic coherences or the encoding of digital information at individual half-cycles to transmit and process information on the Pbit/s scale.

Subcycle tailoring of light transients opens new prospects in ultrafast science. By exerting strong and precisely controlled forces, they can advance attosecond control of electron motion in atoms, molecules or solids to another level. By adjusting the field waveform to encompass a single, intense, field half-cycle (Fig. 15(a)), strong field ionization of atoms and molecules or other nanosystems can be restricted to hundreds of attoseconds, enabling unprecedented accuracy in triggering and clocking atomic scale phenomena such as coherent ultrafast electronic superpositions. This possibility has been recently verified by the attosecond all-optical strong-field ionization of krypton atoms.<sup>40</sup> On the other hand, although the finest feature created on a waveform by conventional terms is only linked to total bandwidth  $\Delta\omega$  of a transient, at the superoctave limit, the effective resolution can be dramatically higher as indicated by the attosecond rise time of the intensity profile of the light transient of Fig. 13(c) as well as by the steep intensity variations between adjacent half-cycles in nearly all light transients presented throughout the paper.

Equally exciting are the envisaged applications of light transients in molecular electronic control. Studies in prototypical molecules based upon  $\phi_{CE}$  controlled pulses,<sup>37</sup> as well as numerous theoretical studies,<sup>90,91</sup> suggest new ways of molecular control that could profoundly benefit from the use of a controlled transient of light to steer the relevant dynamics. Furthermore, superoctave transients may offer the possibility of triggering electronic coherences (through their near ultraviolet or eventually deep ultraviolet spectral components) as well as to drive the excited complex valence shell wavepacket dynamics with its strong NIR components. These applications clearly require the transient to be shaped with precision that goes beyond the limits of the carrier-envelope phase schemes.

Light transients sculpted with subcycle accuracy also hold great promise for attaining the ultimate limits in processing and transportation of information in nanoscale circuitry—an area in which some of the most prominent applications of light control may be applied in the near future. The highest

density of information that can be encoded into a propagating burst of light relates to the potential of tailoring (encoding) the field as well as to characterizing it (decoding). Ultrafast technologies<sup>92</sup> have given important examples of this emerging capability via the control of the intensity profile of picosecond pulses in order to encode bits of information through the switching of temporal features within femtosecond time intervals. Now, the subcycle synthesis of light transients unlocks the potential of extending this capability to its ultimate limits: the encoding of digital information on light transients through the real-time switching of specific half-cycles in a light transient (Fig. 15(b)) at rates that exceed 1 Pbit/s. Extending synthesis technologies into the vacuum ultraviolet and/or the infrared will provide the adequate resolution to encode any potential sequence of bits well beyond the simple illustrative example of Fig. 14(b). Once such a transient is exploited to trigger ultrafast dynamics on a nanoscale system,<sup>93</sup> such as a nanostructure or a nanowire, plasmon oscillations and their propagation can transport the encoded information on the field of the transient at light speeds, opening up new vistas for extending the frontiers of modern electronics and information processing technologies to the PHz realm.

## ACKNOWLEDGMENTS

We thank Ferenc Krausz, M. Hofstetter, U. Kleineberg, Abdallah Azzeer, and Zeyad Alahmed for invaluable contributions to this project. This work was supported by European Research Council grant (Attoelectronics-258501), the Max Planck Society, the Deutsche Forschungsgemeinschaft Cluster of Excellence: Munich Centre for Advanced Photonics ([www.munich-photonics.de](http://www.munich-photonics.de)), and the European Research Training Network ATTOFEL and the King Saud University (KSU) in the framework of the MPQ-KSU Collaboration ([www.mpq-ksu.org](http://www.mpq-ksu.org)).

## APPENDIX A: NUMERICAL PROCEDURE FOR EVALUATING THE FIELD OF A LIGHT TRANSIENT

The following is a description of the particular methods we used for extracting the field transient waveforms from the streaked spectra. First, the centroids of the spectra are evaluated for each EUV-NIR delay, from which the vector potential  $A_{TR}(t)$  is obtained by solving Eq. (1) (ignoring the last term). The vector potential is then numerically differentiated, giving the electric field  $E_{TR}(t) = -\partial_t A_{TR}(t)$  of the transient. Since  $A_{TR}(t)$  is relatively noisy after being extracted from the streaked spectra, we compute its derivative in the frequency domain:

$$\partial_t A_{TR}(t) = \frac{1}{\sqrt{2\pi}} \int_{-\infty}^{\infty} i\omega H(\omega) \tilde{A}_{TR}(\omega) e^{-i\omega t} d\omega, \quad (\text{A1})$$

$$H(\omega) = S\left(\frac{\omega + \Omega}{\delta}\right) S\left(-\frac{\omega - \Omega}{\delta}\right), \quad (\text{A2})$$

$$S(x) = \begin{cases} 0, & x \leq -1/2 \\ \frac{8}{9} \sin^4\left[\frac{2\pi}{3}\left(x + \frac{1}{2}\right)\right], & -1/2 < x \leq 0 \\ -\frac{8}{9} \sin^4\left[\frac{2\pi}{3}\left(x - \frac{1}{2}\right)\right], & 0 < x \leq 1/2 \\ 1, & 1/2 < x \end{cases}, \quad (\text{A3})$$

where  $\tilde{A}_{TR}(\omega)$  is the Fourier transform of  $A_{TR}(t)$ .  $S(x)$  is a smoothed step function that is thrice differentiable. We choose the width of the spectral window,  $\Omega = 0.5/\Delta t_{\min}$ , such that temporal structure finer than  $\Delta t_{\min} = 0.5 fs$  is ignored upon taking the derivative. After obtaining the time series  $E_{TR}(t)$ , it is windowed in the time domain by  $H(t)$  to ensure that it falls to zero at the edges of the overall temporal window. This suppresses noise in the evaluated light transient spectrum, particularly around the high frequency edge. The (real) time series for  $E_{TR}(t)$  is then transformed into an analytic signal  $E_{TR}(t) = \frac{1}{\sqrt{2\pi}} \int_{-\infty}^{\infty} \Theta(\omega) \tilde{E}_{TR}(\omega) e^{-i\omega t} d\omega$ , where  $\tilde{E}_{TR}(\omega)$  is the Fourier transform of  $E_{TR}(t)$ , and  $\Theta(\omega)$  is the Heaviside step function, thus removing the negative frequencies from  $E_{TR}(t)$ . Following this procedure, the electric field is converted from atomic units to  $V/m$  multiplying it by  $\hbar^2/m_e a_0^3 e$ , from which the temporal intensity envelope and phase of the waveform are evaluated and are given by  $c\epsilon_0 |E_{TR}(t)|^2$  and  $\arg[E_{TR}(t)]$ , respectively. The transient's (complex) spectrum is then given by  $S_{TR}(\lambda) = \frac{c\epsilon_0}{2\lambda^2} |\tilde{E}_{TR}(2\pi c/\lambda)|^2 e^{i \arg[\tilde{E}_{TR}(2\pi c/\lambda)]}$ , where  $\tilde{E}_{TR}(\omega)$  is the Fourier transform of the analytical field.

## APPENDIX B: TIME AXIS ADJUSTMENTS BETWEEN CONSECUTIVELY SAMPLED LIGHT TRANSIENTS

According to the principles of high order harmonic generation, the timing of an attosecond burst and that of its driver pulse are intimately related; in particular, the emission of the attosecond burst is linked to the most intense field cycle of the driver field. In our experiments, this implies that if two successively synthesized light transients have considerably different field waveforms, a temporal offset associated to the above mentioned timing may need to be compensated for, prior to their comparison. The tools presented in Sec. II and in Appendix A offer this capability. In a first step, both waveforms are decomposed into their constituent channels as shown in Fig. 12(c). Because the fine timing of pulses in  $\text{Ch}_{\text{VIS}}$  is not adjustable by our synthesizer apparatus—only the optical paths in  $\text{Ch}_{\text{VIS-UV}}$  and  $\text{Ch}_{\text{NIR}}$  can be finely adjusted—their fields can be used to define an absolute time reference and to adjust the temporal axes of successively synthesized light transients with respect to each other. In particular, we temporally translate the field of one of the two light transients in order to overlap their  $\text{Ch}_{\text{VIS}}$  waveforms. Practically, this is achieved at a relative delay that minimizes their rms difference. Adjustments up to 1.6 fs have been introduced in the data shown in Fig. 13(e). The accuracy of this approach has been verified by HHG simulations based on the Lewenstein model and this methodology is quite universal. It can also be used to compensate for other kinds drifts between the attosecond probe and light transients in the measuring apparatus.

- <sup>1</sup>H. Abraham and T. Lemoine, *Compt. Rend.* **129**, 206 (1899).
- <sup>2</sup>T. H. Maiman, *Nature (London)* **187**, 493 (1960).
- <sup>3</sup>M. Dantus, R. M. Bowman, and A. H. Zewail, *Nature (London)* **343**, 737 (1990).
- <sup>4</sup>Ahmed H. Zewail, *J. Phys. Chem. A* **104**, 5660 (2000).
- <sup>5</sup>M. Hentschel, R. Kienberger, Ch. Spielmann, G. A. Reider, N. Milosevic, T. Brabec, P. Corkum, U. Heinzmann, M. Drescher, and F. Krausz, *Nature (London)* **414**, 509 (2001).
- <sup>6</sup>Y. Mairesse, A. de Bohan, L. J. Frasinski, H. Merdji, L. C. Dinu, P. Monchicourt, P. Breger, M. Kovačev, R. Taïeb, B. Carré, H. G. Muller, P. Agostini, and P. Salieres, *Science* **302**, 1540 (2003).
- <sup>7</sup>M. Drescher, M. Hentschel, R. Kienberger, M. Uiberacker, V. Yakovlev, A. Scrinzi, Th. Westerwalbesloh, U. Kleineberg, U. Heinzmann, and F. Krausz, *Nature (London)* **419**, 803 (2002).
- <sup>8</sup>R. Kienberger, E. Goulielmakis, M. Uiberacker, A. Baltuska, V. Yakovlev, F. Bammer, A. Scrinzi, Th. Westerwalbesloh, U. Kleineberg, U. Heinzmann, M. Drescher, and F. Krausz, *Nature (London)* **427**, 817 (2004).
- <sup>9</sup>E. Goulielmakis, Z.-H. Loh, A. Wirth, R. Santra, N. Rohringer, V. S. Yakovlev, S. Zherebtsov, T. Pfeifer, A. M. Azzeer, M. F. Kling, S. R. Leone, and F. Krausz, *Nature (London)* **466**, 739 (2010).
- <sup>10</sup>C. Froehly, B. Colombeau, and M. Vampouille, in *Progress in Optics*, edited by E. Wolf (Elsevier, 1983), Vol. 20, p. 63.
- <sup>11</sup>A. M. Weiner, *Rev. Sci. Instrum.* **71**, 1929 (2000).
- <sup>12</sup>O. E. Martinez, J. P. Gordon, and R. L. Fork, *J. Opt. Soc. Am. A* **1**, 1003 (1984).
- <sup>13</sup>E. Treacy, *IEEE J. Quantum Electron.* **5**, 454 (1969).
- <sup>14</sup>A. M. Weiner, D. E. Leaird, J. S. Patel, and J. R. Wullert II, *IEEE J. Quantum Electron.* **28**, 908 (1992).
- <sup>15</sup>A. Weiner, *Ultrafast Optics* (Wiley, New Jersey, 2009).
- <sup>16</sup>S. T. Cundiff and A. M. Weiner, *Nat. Photon.* **4**, 760 (2010).
- <sup>17</sup>F. Verluise, V. Laude, Z. Cheng, Ch. Spielmann, and P. Tournais, *Opt. Lett.* **25**, 575 (2000).
- <sup>18</sup>T. Brixner and G. Gerber, *Opt. Lett.* **26**, 557 (2001).
- <sup>19</sup>W. S. Warren, H. Rabitz, and M. Dahleh, *Science* **259**, 1581 (1993).
- <sup>20</sup>P. W. Brumer and M. Shapiro, *Principles of the Quantum Control of Molecular Processes* (Wiley-Interscience, New Jersey, 2003).
- <sup>21</sup>T. Brixner, N. H. Damrauer, and G. Gerber, in *Advances in Atomic, Molecular, and Optical Physics*, edited by B. Benjamin and W. Herbert (Academic, 2001), Vol. 46, pp. 1.
- <sup>22</sup>A. Assion, T. Baumert, M. Bergt, T. Brixner, B. Kiefer, V. Seyfried, M. Strehle, and G. Gerber, *Science* **282**, 919 (1998).
- <sup>23</sup>M. Wollenhaupt, V. Engel, and T. Baumert, *Ann. Rev. Phys. Chem.* **56**, 25 (2005).
- <sup>24</sup>S. T. Cundiff, *J. Phys. D: Appl. Phys.* **35**, R43 (2002).
- <sup>25</sup>L. Xu, Ch. Spielmann, F. Krausz, and R. Szipöcs, *Opt. Lett.* **21**, 1259 (1996).
- <sup>26</sup>J. Reichert, R. Holzwarth, Th. Udem, and T. W. Hänsch, *Opt. Commun.* **172**, 59 (1999).
- <sup>27</sup>A. Apolonski, A. Poppe, G. Tempea, Ch. Spielmann, Th. Udem, R. Holzwarth, T. W. Hänsch, and F. Krausz, *Phys. Rev. Lett.* **85**, 740 (2000).
- <sup>28</sup>D. J. Jones, S. A. Diddams, J. K. Ranka, A. Stentz, R. S. Windeler, J. L. Hall, and S. T. Cundiff, *Science* **288**, 635 (2000).
- <sup>29</sup>Th. Udem, R. Holzwarth, and T. W. Hänsch, *Nature (London)* **416**, 233 (2002).
- <sup>30</sup>S. Koke, C. Grebing, H. Frei, A. Anderson, A. Assion, and G. Steinmeyer, *Nat. Photon.* **4**, 462 (2010).
- <sup>31</sup>T. W. Hänsch, *Rev. Mod. Phys.* **78**, 1297 (2006).
- <sup>32</sup>A. Baltuska, Th. Udem, M. Uiberacker, M. Hentschel, E. Goulielmakis, Ch. Gohle, R. Holzwarth, V. S. Yakovlev, A. Scrinzi, T. W. Hänsch, and F. Krausz, *Nature (London)* **421**, 611 (2003).
- <sup>33</sup>F. Krausz and M. Ivanov, *Rev. Mod. Phys.* **81**, 163 (2009).
- <sup>34</sup>E. Goulielmakis, M. Schultze, M. Hofstetter, V. S. Yakovlev, J. Gagnon, M. Uiberacker, A. L. Aquila, E. M. Gullikson, D. T. Attwood, R. Kienberger, F. Krausz, and U. Kleineberg, *Science* **320**, 1614 (2008).
- <sup>35</sup>E. Goulielmakis, M. Uiberacker, R. Kienberger, A. Baltuska, V. Yakovlev, A. Scrinzi, Th. Westerwalbesloh, U. Kleineberg, U. Heinzmann, M. Drescher, and F. Krausz, *Science* **305**, 1267 (2004).
- <sup>36</sup>J. Mauritsson, T. Remetter, M. Swoboda, K. Klünder, A. L'Huillier, K. J. Schafer, O. Ghafur, F. Kelkensberg, W. Siu, P. Johnsson, M. J. J. Vrakking, I. Znakovskaya, T. Uphues, S. Zherebtsov, M. F. Kling, F. Lépine, E. Benedetti, F. Ferrari, G. Sansone, and M. Nisoli, *Phys. Rev. Lett.* **105**, 053001 (2010).
- <sup>37</sup>M. F. Kling, Ch. Siedschlag, A. J. Verhoef, J. I. Khan, M. Schultze, Th. Uphues, Y. Ni, M. Uiberacker, M. Drescher, F. Krausz, and M. J. J. Vrakking, *Science* **312**, 246 (2006).
- <sup>38</sup>G. Sansone, E. Benedetti, F. Calegari, C. Vozzi, L. Avaldi, R. Flammini, L. Poletto, P. Villorosi, C. Altucci, R. Velotta, S. Stagira, S. De Silvestri, and M. Nisoli, *Science* **314**, 443 (2006).
- <sup>39</sup>A. L. Cavalieri, N. Muller, Th. Uphues, V. S. Yakovlev, A. Baltuska, B. Horvath, B. Schmidt, L. Blumel, R. Holzwarth, S. Hendel, M. Drescher, U. Kleineberg, P. M. Echenique, R. Kienberger, F. Krausz, and U. Heinzmann, *Nature (London)* **449**, 1029 (2007).
- <sup>40</sup>A. Wirth, M. Th. Hassan, I. Grguraš, J. Gagnon, A. Moulet, T. T. Luu, S. Pabst, R. Santra, Z. A. Alahmed, A. M. Azzeer, V. S. Yakovlev, V. Pervak, F. Krausz, and E. Goulielmakis, *Science* **334**, 195 (2011).
- <sup>41</sup>S. E. Harris and A. V. Sokolov, *Phys. Rev. Lett.* **81**, 2894 (1998).
- <sup>42</sup>A. V. Sokolov, D. R. Walker, D. D. Yavuz, G. Y. Yin, and S. E. Harris, *Phys. Rev. Lett.* **85**, 562 (2000).
- <sup>43</sup>T. Suzuki, M. Hirai, and M. Katsuragawa, *Phys. Rev. Lett.* **101**, 243602 (2008).
- <sup>44</sup>J. Q. Liang, M. Katsuragawa, F. Le Kien, and K. Hakuta, *Phys. Rev. Lett.* **85**, 2474 (2000).
- <sup>45</sup>Z.-M. Hsieh, C.-J. Lai, H.-S. Chan, S.-Y. Wu, C.-K. Lee, W.-J. Chen, C.-L. Pan, F.-G. Yee, and A. H. Kung, *Phys. Rev. Lett.* **102**, 213902 (2009).
- <sup>46</sup>S. Baker, I. A. Walmsley, J. W. G. Tisch, and J. P. Marangos, *Nat. Photon.* **5**, 664 (2011).
- <sup>47</sup>H.-S. Chan, Z.-M. Hsieh, W.-H. Liang, A. H. Kung, C.-K. Lee, C.-J. Lai, R.-P. Pan, and L.-H. Peng, *Science* **331**, 1165 (2011).
- <sup>48</sup>R. K. Shelton, L.-S. Ma, H. C. Kapteyn, M. M. Murnane, J. L. Hall, and J. Ye, *Science* **293**, 1286 (2001).
- <sup>49</sup>M. Yamashita, K. Yamane, and R. Morita, *IEEE J. Sel. Top Quantum Electron.* **12**, 213 (2006).
- <sup>50</sup>S. Rausch, T. Binhammer, A. Harth, F. X. Krtnr, and U. Morgner, *Opt. Express* **16**, 17410 (2008).
- <sup>51</sup>G. Krauss, S. Lohss, T. Hanke, A. Sell, S. Eggert, R. Huber, and A. Leitenstorfer, *Nat. Photon.* **4**, 33 (2010).
- <sup>52</sup>S.-W. Huang, G. Cirmi, J. Moses, K.-H. Hong, S. Bhardwaj, J. R. Birge, L.-J. Chen, E. Li, B. J. Eggleton, G. Cerullo, and F. X. Kartner, *Nat. Photon.* **5**, 475 (2011).
- <sup>53</sup>E. Goulielmakis, V. S. Yakovlev, A. L. Cavalieri, M. Uiberacker, V. Pervak, A. Apolonski, R. Kienberger, U. Kleineberg, and F. Krausz, *Science* **317**, 769 (2007).
- <sup>54</sup>M. Maier, W. Kaiser, and J. A. Giordmaine, *Phys. Rev. Lett.* **17**, 1275 (1966).
- <sup>55</sup>C. Iaconis and I. A. Walmsley, *Opt. Lett.* **23**, 792 (1998).
- <sup>56</sup>C. Yan and J.-C. Diels, *J. Opt. Soc. Am. B* **8**, 1259 (1991).
- <sup>57</sup>I. A. Walmsley and V. Wong, *J. Opt. Soc. Am. B* **13**, 2453 (1996).
- <sup>58</sup>R. Trebino and D. J. Kane, *J. Opt. Soc. Am. A* **10**, 1101 (1993).
- <sup>59</sup>M. Nisoli, S. De Silvestri, O. Svelto, R. Szipöcs, K. Ferencz, Ch. Spielmann, S. Sartania, and F. Krausz, *Opt. Lett.* **22**, 522 (1997).
- <sup>60</sup>A. L. Cavalieri, E. Goulielmakis, B. Horvath, W. Helml, M. Schultze, M. Fieβ, V. Pervak, L. Veisz, V. S. Yakovlev, M. Uiberacker, A. Apolonski, F. Krausz, and R. Kienberger, *New J. Phys.* **9**, 242 (2007).
- <sup>61</sup>U. Graf, M. Fieβ, M. Schultze, R. Kienberger, F. Krausz, and E. Goulielmakis, *Opt. Express* **16**, 18956 (2008).
- <sup>62</sup>R. Szipöcs, K. Ferencz, Ch. Spielmann, and F. Krausz, *Opt. Lett.* **19**, 201 (1994).
- <sup>63</sup>V. Pervak, *Appl. Opt.* **50**, C55 (2011).
- <sup>64</sup>M. Z. Aleksei, *Phys.-Usp.* **49**, 605 (2006).
- <sup>65</sup>G. P. Agrawal, *Nonlinear Fiber Optics* (Academic, Baltimore, MD, 2006).
- <sup>66</sup>E. E. Serebryannikov *et al.*, *New J. Phys.* **10**, 093001 (2008).
- <sup>67</sup>M. Schultze, A. Wirth, I. Grguras, M. Uiberacker, T. Uphues, A. J. Verhoef, J. Gagnon, M. Hofstetter, U. Kleineberg, E. Goulielmakis, and F. Krausz, *J. Electron Spectrosc. Relat. Phenom.* **184**, 68 (2011).
- <sup>68</sup>T. Fuji, J. Rauschenberger, Ch. Gohle, A. Apolonski, Th. Udem, V. S. Yakovlev, G. Tempea, T. W. Hänsch, and F. Krausz, *New J. Phys.* **7**, 116 (2005).
- <sup>69</sup>J. N. Sweetser, D. N. Fittinghoff, and R. Trebino, *Opt. Lett.* **22**, 519 (1997).
- <sup>70</sup>A. V. Tikhonravov, M. K. Trubetskov, and G. W. DeBell, *Appl. Opt.* **35**, 5493 (1996).
- <sup>71</sup>V. Pervak, "Multi-octave dispersive optics" (unpublished).
- <sup>72</sup>J. F. Whitaker, J. A. Valdmanis, M. Y. Frankel, S. Gupta, J. M. Chwalek, and G. A. Mourou, *Microelectron. Eng.* **12**, 369 (1990).
- <sup>73</sup>V. S. Yakovlev, J. Gagnon, N. Karpowicz, and F. Krausz, *Phys. Rev. Lett.* **105**, 073001 (2010).

- <sup>74</sup>J. Itatani, F. Quéré, G. L. Yudin, M. Yu Ivanov, F. Krausz, and P. B. Corkum, *Phys. Rev. Lett.* **88**, 173903 (2002).
- <sup>75</sup>M. Kitzler, N. Milosevic, A. Scrinzi, F. Krausz, and T. Brabec, *Phys. Rev. Lett.* **88**, 173904 (2002).
- <sup>76</sup>X. Feng, S. Gilbertson, H. Mashiko, H. Wang, S. D. Khan, M. Chini, Y. Wu, K. Zhao, and Z. Chang, *Phys. Rev. Lett.* **103**, 183901 (2009).
- <sup>77</sup>H. Mashiko, M. J. Bell, A. R. Beck, M. J. Abel, P. M. Nagel, C. P. Steiner, J. Robinson, D. M. Neumark, and S. R. Leone, *Opt. Express* **18**, 25887 (2010).
- <sup>78</sup>R. Trebino, K. W. DeLong, D. N. Fittinghoff, J. N. Sweetser, M. A. Krumbugel, B. A. Richman, and D. J. Kane, *Rev. Sci. Instrum.* **68**, 3277 (1997).
- <sup>79</sup>Y. Mairesse and F. Quéré, *Phys. Rev. A* **71**, 011401 (2005).
- <sup>80</sup>J. Gagnon, E. Goulielmakis, and V. S. Yakovlev, *Appl. Phys. B: Lasers Opt.* **92**, 25 (2008).
- <sup>81</sup>M. Ferray, A. L' Huillier, X. F. Li, L. A. Lompre, G. Mainfray, and C. Manus, *J. Phys. B* **21**, L31 (1988).
- <sup>82</sup>J. Gagnon and V. Yakovlev, *Appl. Phys. B: Lasers Opt.* **103**, 303 (2011).
- <sup>83</sup>M. Schultze, M. Fieß, N. Karpowicz, J. Gagnon, M. Korbman, M. Hofstetter, S. Neppl, A. L. Cavalieri, Y. Komninos, Th. Mercouris, C. A. Nicolaides, R. Pazourek, S. Nagele, J. Feist, J. Burgdörfer, A. M. Azzeer, R. Ernstorfer, R. Kienberger, U. Kleineberg, E. Goulielmakis, F. Krausz, and V. S. Yakovlev, *Science* **328**, 1658 (2010).
- <sup>84</sup>C. Dorrer and I. A. Walmsley, *J. Opt. Soc. Am. B* **19**, 1019 (2002).
- <sup>85</sup>F. Reiter, U. Graf, E. E. Serebryannikov, W. Schweinberger, M. Fiess, M. Schultze, A. M. Azzeer, R. Kienberger, F. Krausz, A. M. Zheltikov, and E. Goulielmakis, *Phys. Rev. Lett.* **105**, 243902 (2010).
- <sup>86</sup>F. Reiter, U. Graf, M. Schultze, W. Schweinberger, H. Schröder, N. Karpowicz, A. Mohammed Azzeer, R. Kienberger, F. Krausz, and E. Goulielmakis, *Opt. Lett.* **35**, 2248 (2010).
- <sup>87</sup>C. Homann, N. Krebs, and E. Riedle, *Appl. Phys. B: Lasers Opt.* **104**, 783 (2011).
- <sup>88</sup>T. Nagy and P. Simon, *Opt. Express* **17**, 8144 (2009).
- <sup>89</sup>T. Fuji and T. Suzuki, *Opt. Lett.* **32**, 3330 (2007).
- <sup>90</sup>F. Remacle, M. Nest, and R. D. Levine, *Phys. Rev. Lett.* **99**, 183902 (2007).
- <sup>91</sup>P. von den Hoff, R. Siemering, M. Kowalewski, and R. de Vivie-Riedle, *IEEE J. Sel. Top Quantum Electron* **18**, 119 (2012).
- <sup>92</sup>D. E. Leaird and A. M. Weiner, *Opt. Lett.* **24**, 853 (1999).
- <sup>93</sup>E. Ozbay, *Science* **311**, 189 (2006).